

PACS and SPIRE range spectroscopy of cool, evolved stars[★]

D. Nicolaes^{1,2}, M. A. T. Groenewegen¹, P. Royer², R. Lombaert³, T. Danilovich², and L. Decin²

¹ Koninklijke Sterrenwacht van België, Ringlaan 3, 1180 Brussel, Belgium
e-mail: marting@oma.be

² Instituut voor Sterrenkunde, KU Leuven, Celestijnenlaan 200D, 3001 Leuven, Belgium

³ Onsala Space Observatory, Department of Earth and Space Sciences, Chalmers University of Technology, 439 92 Onsala, Sweden

Received 5 April 2018 / Accepted 20 July 2018

ABSTRACT

Context. At the end of their lives AGB stars are prolific producers of dust and gas. The details of this mass-loss process are still not understood very well. *Herschel* PACS and SPIRE spectra which cover the wavelength range from ~ 55 to $670 \mu\text{m}$ almost continuously, offer a unique way of investigating properties of AGB stars in general and the mass-loss process in particular as this is the wavelength region where dust emission is prominent and molecules have many emission lines.

Aims. We present the community with a catalogue of AGB stars and red supergiants (RSGs) with PACS and/or SPIRE spectra reduced according to the current state of the art.

Methods. The *Herschel* interactive processing environment (HIPE) software with the latest calibration is used to process the available PACS and SPIRE spectra of 40 evolved stars. The SPIRE spectra of some objects close to the Galactic plane require special treatment because of the weaker fluxes in combination with the strong and complex background emission at those wavelengths. The spectra are convolved with the response curves of the PACS and SPIRE bolometers and compared to the fluxes measured in imaging data of these sources. Custom software is used to identify lines in the spectra, and to determine the central wavelengths and line intensities. Standard molecular line databases are used to associate the observed lines. Because of the limited spectral resolution of the PACS and SPIRE spectrometers (~ 1500), several known lines are typically potential counterparts to any observed line. To help identifications in follow-up studies the relative contributions in line intensity of the potential counterpart lines are listed for three characteristic temperatures based on local thermodynamic equilibrium (LTE) calculations and assuming optically thin emission.

Results. The following data products are released: the reduced spectra, the lines that are measured in the spectra with wavelength, intensity, potential identifications, and the continuum spectra, i.e. the full spectra with all identified lines removed. As simple examples of how this data can be used in future studies we have fitted the continuum spectra with three power laws (two wavelength regimes covering PACS, and one covering SPIRE) and find that the few OH/IR stars seem to have significantly steeper slopes than the other oxygen- and carbon-rich objects in the sample, possibly related to a recent increase in mass-loss rate. As another example we constructed rotational diagrams for CO (and HCN for the carbon stars) and fitted a two-component model to derive rotational temperatures.

Key words. stars: AGB and post-AGB – stars: mass-loss – infrared: stars

1. Introduction

The initial mass of a star determines its evolution and therefore also the final stages of its life. After leaving the main sequence, stars with an initial mass between $\sim 0.8 M_{\odot}$ and $\sim 8 M_{\odot}$ will climb the red giant and asymptotic giant branches (RGB and AGB), while more massive stars will go through a supergiant phase. During the AGB and supergiant phases, mass loss dominates the evolution and a star will expel a significant part of its initial mass via a stellar wind. The ejection of stellar material creates a cool and extended circumstellar envelope (CSE) containing dust grains and molecular gas-phase species. In this way, AGB and supergiant stars contribute significantly to the return of gas and dust to the interstellar medium (ISM) from which new generations of stars are born.

From a qualitative point of view it is known that the mass-loss processes are closely related to the intrinsic characteristics of the star, like mass, luminosity, variability and chemical

composition (Habing & Olofsson 2003; Höfner & Olofsson 2018). Despite extensive research efforts, stellar evolution models are not yet able to quantitatively predict the mass-loss history of AGB or supergiant stars from first principles. The details of the physical processes that govern the mass-loss dynamics and its variation in time remain unclear. A fulfilling description of the different key chemical processes that determine the wind's chemical composition is also lacking. Observationally characterising the full dynamical and chemical structure of the CSE from the stellar atmosphere up to the most outer parts of the wind will be helpful in clarifying the underlying mass-loss mechanism by providing models with as many constraints as possible.

The *Herschel* Space observatory (hereafter *Herschel*; Pilbratt et al. 2010) plays a key role in these analyses. *Herschel* collected data at far-infrared and submillimetre wavelengths which cover a large part of the wavelength region where the gas and dust in the extended CSE emit most of their continuum and line radiation. In this way, *Herschel* bridges the gap between ground-based instruments which are only able to obtain data in selected atmospheric windows at shorter (near- and mid-infrared) and those that can obtain data at longer (millimetre and radio) wavelengths. Due to the good spatial and spectral

[★] The reduced spectra and the line subtracted spectra as well as Table E.1 are only available at the CDS via anonymous ftp to cdsarc.u-strasbg.fr (130.79.128.5) or via <http://cdsweb.u-strasbg.fr/cgi-bin/qcat?J/A+A/618/A143>

resolution of the instruments on board, *Herschel* revealed new insights in the structure and chemistry of CSEs.

This paper presents consistent and carefully reduced data of the PACS and SPIRE instruments on board *Herschel* of all AGB and supergiants stars that were observed by the PACS and SPIRE spectrometers.

A large fraction of the data presented here were obtained within the framework of the Mass loss of Evolved StarS (MESS) guaranteed time key programme (Groenewegen et al. 2011) and were published in part in earlier publications, using the best available data reduction at that time. Royer et al. (2010) presented PACS and SPIRE data on VY CMa and an initial model for the CSE, while a more elaborate analysis was presented by Matsuura et al. (2014), using radiative transfer models to fit the ^{12}CO , ^{13}CO , SiO and water lines in these spectra and to derive mass-loss rates (MLRs) and the gas temperature profile in the CSE. Decin et al. (2010a) presented the detection of high-excitation lines of H_2O in the carbon star CW Leo (IRC +10 216) and suggested that interstellar UV photons could penetrate deep into the clumpy CSE, an alternative scenario to the one proposed by Melnick et al. (2001) of the vaporisation of a collection of orbiting icy bodies based on the detection of a single line with SWAS. This analysis was later extended by Lombaert et al. (2016) who studied the water lines in 18 C stars (including six targets from the MESS program). Danilovich et al. (2017) studied the water isotopologues in four M-type stars (R Dor, IK Tau, R Cas, and W Hya) including data from MESS. Other studies analysed molecular line data (based partly on MESS data) for CW Leo (De Beck et al. 2012), OH 127.8 +0.0 (Lombaert et al. 2013), W Hya (Khoury et al. 2014a,b), W Aql (Danilovich et al. 2017), and R Dor (Van de Sande et al. 2018), typically using radiative transfer models to derive properties of the CSE, such as abundances or abundance profiles.

The present paper also discusses PACS and SPIRE imaging data, but only for the targets which have spectroscopic data. Initial PACS and SPIRE photometry was presented in Groenewegen et al. (2011), but not all observations had been completed at that time. An overview of the PACS imaging of all 78 MESS targets can be found in Cox et al. (2012), showing and discussing, amongst other things, four different classes of wind-ISM interaction observed in $\sim 40\%$ of the sample.

MESS imaging data have been discussed in more detail for individual objects as well. Ladjal et al. (2010) discussed the bow shock around CW Leo seen in SPIRE data (discovered a few months earlier in GALEX UV data by Sahai & Chronopoulos 2010) while Decin et al. (2011) presented the discovery of multiple shells around this object. Decin et al. (2012) discussed the detection of the bow shock around Betelgeuse, while the interesting class of C-rich objects with detached shells have been discussed in Kerschbaum et al. (2010; AQ And, U Ant, and TT Cyg) and Mećina et al. (2014; S Sct and RT Cap). The CSE of stars showing binary interaction have been discussed by Mayer et al. (2013; R Aqr and W Aql) and Mayer et al. (2014; π Gru).

The paper is structured as follows. Section 2 presents the data sample and describes the adopted data reduction and processing strategy. In Sect. 3 the flux level of the PACS and SPIRE spectra is compared to that measured independently by the PACS and SPIRE bolometer arrays in order to have an estimate of the flux level consistency and to identify possible problematic stars or wavelength regions. In Sect. 4.1 the strategy to extract the molecular lines is outlined, while Sect. 4.4 describes the determination of the dust continua. Section 4 discusses the identification of the molecular lines, the construction of rotational diagrams, and the

Table 1. Basic properties of the PACS and SPIRE spectrometers.

Band/range	FWHM of an unresolved line (μm)	PSF (FWHM in $''$)
B2A-B3A (55–72 μm)	0.021–0.013	~ 9.0
B2B (72–105 μm)	0.039–0.028	9.0–9.3
R (105–210 μm)	0.10–0.13	9.3–14
SSW (191–318 μm)	0.15–0.40	16.5–20.5
SLW (294–671 μm)	0.35–1.8	31.0–42.8

derivation of rotational temperatures for CO (and HCN for the carbon stars), and the slopes of the dust continua. Section 5 summarises this paper.

When this paper was submitted we became aware of the article by Ramos-Medina et al. (2018) that presents PACS range spectroscopy of 114 evolved stars. The sample they consider also includes planetary nebula and post-AGB stars and is therefore larger than ours. For the reader it is important to know that our effort and theirs were carried out independently of each other.

2. Data

2.1. Target sample and observations

The sample consists of 37 AGB and 3 RSG stars observed by the PACS (Poglitsch et al. 2010)¹ and SPIRE (Griffin et al. 2010)² instruments on board *Herschel*. As this paper focuses on spectroscopy some of the main properties of the spectrometers are recalled below. The PACS spectrometer field of view consists of 5×5 spatial pixels (spaxels) of $9.4 \times 9.4''$ each on the sky. Background subtraction is done using a classical chop-nod technique, with chopper throws of 1.5, 3.0 or 6.0'.

The SPIRE Fourier Transform Spectrometer (FTS) consists of two hexagonally close-packed arrays with 37 detectors in the short-wavelength array (SSW) and 19 in the long-wavelength array (SLW). The full instrument field of view is 2.6' in diameter. The size of the beam and the resolution (represented as the width of an unresolved line) depend on wavelength and are given in Table 1.

The main characteristics of the 40 targets are listed in Table 2. Distances and MLRs are representative values taken from the literature and are not explicitly used in this paper. Together with the pulsation type and chemical type these parameters illustrate the diversity of the sample. The expansion velocities are used in the paper (see Sect. 4.2) to correct the central wavelength of the observed molecular lines to rest wavelengths.

More precisely, the *Herschel* Science Archive (HSA) was searched and all AGB and RSG targets with a PACS spectrum observed in spectral energy distribution (SED) mode were selected. In this mode, the full PACS wavelength range is covered by combining at least two astronomical observation requests (AORs). The three different SED-AOR options are³: B2A + short R1 ([51–73] μm + [102–146] μm), B2B + long R1 ([70–105] μm + [140–220] μm), and B3A + long R1 ([47–73] μm + [140–219] μm). The bluest and reddest parts of

¹ Also see the PACS observers manual at http://herschel.esac.esa.int/Docs/PACS/pdf/pacs_om.pdf or http://herschel.esac.esa.int/Docs/PACS/html/pacs_om.html

² Also see the SPIRE handbook at herschel.esac.esa.int/Docs/SPIRE/spire_handbook.pdf or http://herschel.esac.esa.int/Docs/SPIRE/html/spire_om.html

³ Nomenclature and wavelength ranges following the PACS observers manual Sect. 6.2.7.1. Short and long R1 are sometimes also designated R1A and R1B, respectively.

Table 2. Basic properties of the sample stars.

IRAS name	Identifier	Chem. type	Puls. type	Distance (Ref.) (kpc)	v_{LSR} (Ref.) (km s^{-1})	\dot{M} (Ref.) ($M_{\odot} \text{yr}^{-1}$)
<i>AGB-stars</i>						
01037+1219	WX Psc	M	Mira	0.74 (1)	9.0 (13)	4.0×10^{-5} (20)
01246–3248	R Scl	C	SRb	0.27 (2)	–19.0 (14)	1.0×10^{-6} (21)
01304+6211	OH 127.8+0.0	M	Mira	2.10 (3)	–55.0 (13)	5.0×10^{-5} (3)
02168–0312	ρ Cet	M	Mira	0.09 (2)	46.5 (15)	2.5×10^{-7} (13)
03507+1115	IK Tau, NML Tau	M	Mira	0.26 (4)	34.0 (16)	1.0×10^{-5} (20)
04361–6210	R Dor	M	SRb	0.05 (2)	7.0 (16)	1.3×10^{-7} (20)
04566+5606	TX Cam	M	Mira	0.39 (1)	11.4 (16)	1.0×10^{-5} (20)
09425–6040	...	C	Mira	1.30 (5)	15.0 (5)	2.0×10^{-6} (5)
09452+1330	CW Leo	C	Mira	0.12 (6)	–26.0 (15)	1.5×10^{-5} (20)
10131+3049	RW LMi, CIT6	C	SRa	0.32 (7)	–1.8 (13)	6.0×10^{-6} (20)
10491–2059	V Hya	C	SRa	0.60 (7)	–16.0 (17)	8.3×10^{-6} (7)
13462–2807	W Hya	M	Mira	0.10 (2)	40.5 (16)	1.3×10^{-7} (22)
15194–5115	Π Lup	C	Mira	0.59 (7)	–5.5 (14)	1.7×10^{-5} (14)
16011+4722	X Her	M	SRb	0.14 (2)	–73.0 (15)	1.5×10^{-7} (23)
17411–3154	AFGL 5379, OH 357.3–1.3	M	Mira	0.99 (1)	–21.2 (13)	2.0×10^{-4} (8)
18257–1000	OH 21.5+0.5	M	Mira	2.50 (8)	115.0 (13)	2.6×10^{-4} (8)
18348–0526	OH 26.5+0.6	M	Mira	1.30 (9)	29.0 (15)	2.6×10^{-4} (8)
18460–0254	OH 30.1–0.7	M	Mira	1.75 (8)	100.0 (13)	2.2×10^{-4} (8)
18488–0107	OH 32.0–0.5	M	Mira	3.90 (8)	75.0 (13)	3.6×10^{-4} (8)
18498–0017	OH 32.8–0.3	M	Mira	4.30 (8)	60.0 (13)	3.1×10^{-4} (8)
19039+0809	R Aql	M	Mira	0.42 (2)	46.0 (18)	3.5×10^{-6} (24)
19067+0811	OH 42.3–0.1	M	Mira	3.80 (8)	60.0 (13)	2.7×10^{-4} (12)
19126–0708	W Aql	S	Mira	0.68 (10)	–27.5 (15)	2.2×10^{-6} (12)
19474–0744	GY Aql	M	Mira	0.22 (2)	33.0 (18)	6.0×10^{-6} (11)
19486+3247	χ Cyg	S	Mira	0.18 (2)	10.0 (15)	3.8×10^{-7} (20)
19550–0201	RR Aql	M	Mira	0.52 (2)	28.0 (14)	2.4×10^{-6} (14)
20038–2722	V1943 Sgr	M	SRb	0.20 (2)	–15.0 (14)	9.9×10^{-8} (14)
20072+3116	AFGL 2513	C	Mira	1.76 (7)	17.8 (7)	2.1×10^{-5} (7)
20077–0625	IRC –10 529, V1300 Aql	M	Mira	0.66 (11)	–18.0 (14)	3.0×10^{-5} (20)
20248–2825	T Mic	M	SRb	0.21 (2)	25.0 (19)	8.0×10^{-8} (24)
20396+4757	V Cyg	C	Mira	0.35 (2)	15.0 (13)	9.0×10^{-7} (20)
21088+6817	T Cep	M	Mira	0.19 (2)	–2.0 (14)	9.1×10^{-8} (14)
21439–0226	EP Aqr	M	SRb	0.11 (2)	–34.0 (14)	3.1×10^{-7} (13)
22196–4612	π Gru	S	SRb	0.16 (2)	–12.0 (14)	8.5×10^{-7} (13)
23166+1655	LL Peg, AFGL 3068	C	Mira	1.00 (7)	–31.0 (13)	1.0×10^{-5} (20)
23320+4316	LP And, AFGL 3116	C	Mira	0.78 (7)	–17.0 (13)	1.5×10^{-5} (20)
23558+5106	R Cas	M	Mira	0.13 (2)	25.0 (16)	5.0×10^{-7} (20)
<i>Red Super Giants</i>						
05524+0723	α Ori	M	SRc	0.15 (2)	3.5 (13)	2.0×10^{-6} (25)
07209–2540	VY CMa	M	Lc	1.17 (12)	17.0 (15)	3.0×10^{-4} (25)
...	NML Cyg	M	...	1.61 (12)	–1.0 (15)	8.7×10^{-5} (13)

Notes. The sources are listed by the IRAS identifier. Column 1 lists the IRAS name, when available, and Col. 2 some common names. Column 3 gives the chemical type (M, S, or C), and Col. 4 the variability type. Columns 5–7 give the distance, velocity of the object (on the local standard of rest scale), and MLR, with the reference between parenthesis.

References. (1) Olivier et al. (2001), (2) van Leeuwen (2007), (3) Lombaert et al. (2013), (4) Richards et al. (2012), (5) Molster et al. (2001), (6) Groenewegen et al. (2012), (7) Groenewegen et al. (2002), (8) Justtanont et al. (2006), (9) van Langevelde et al. (1990), (10) Groenewegen & de Jong (1998), (11) Loup et al. (1993), (12) Reid et al. (2014), (13) De Beck et al. (2010), (14) Danilovich et al. (2015), (15) de Vicente et al. (2016), (16) Danilovich et al. (2016), (17) Sahai et al. (2009), (18) Desmurs et al. (2014), (19) González Delgado et al. (2003), (20) Schöier et al. (2013), (21) Maercker et al. (2014), (22) Khouri et al. (2014a), (23) Olofsson et al. (2002), (24) Knapp & Morris (1985), (25) Smith et al. (2009).

the spectrum cannot be reliably calibrated (see Sect. 2.2.1), and flux calibrated data is available from 55 to 95 and from 102 to $190 \mu\text{m}$.

The PACS spectra were complemented with single pointed SPIRE FTS data, when available. A complete SPIRE spectrum spans a wavelength range from 190 to $670 \mu\text{m}$ covered by two

bands: the SSW band (191–317 μm) and the SLW band (294–670 μm), which are simultaneously observed within 1 AOR.

Additionally, the HSA was searched for PACS and SPIRE photometric maps, which will be used as reference data. PACS data are simultaneously obtained in the blue ($\lambda_{\text{ref}} = 70 \mu\text{m}$) and red ($\lambda_{\text{ref}} = 160 \mu\text{m}$), or simultaneously in the green ($\lambda_{\text{ref}} = 100 \mu\text{m}$) and red bands, while SPIRE maps are obtained in all three bands at once: the PSW ($\lambda_{\text{ref}} = 250 \mu\text{m}$), the PMW ($\lambda_{\text{ref}} = 350 \mu\text{m}$) and the PLW ($\lambda_{\text{ref}} = 500 \mu\text{m}$) band. When imaging is performed in PACS-SPIRE parallel mode the PACS blue and red band, and all SPIRE bands are simultaneously covered.

Details about the observations can be found in Table A.1. The Mass loss of Evolved StarS (MESS) guaranteed time (GT) key programme (Groenewegen 2007; Groenewegen et al. 2011) is the main contributor to the sample. The aim of the programme was to study the mass-loss processes in evolved stars and the structure of their circumstellar environments. The stars in the MESS sample were specifically chosen to be representative of the various types of objects in terms of spectral type (covering the oxygen-rich stars, S-stars, carbon stars), variability type (L, SR, Mira), and MLR (from 10^{-7} to $\sim 3 \times 10^{-4} M_{\odot} \text{yr}^{-1}$). The programme provided PACS spectra for 24 of our 40 targets, most of them obtained in the standard SED mode and combining the (B2A + short R1) and (B2B + long R1) bands. The PACS spectroscopic data of CW Leo were obtained in a 3×1 raster, however, only the on-source pointed observation was selected for our study. Furthermore, a non-standard version of the PACS-SED observing mode was adopted to CW Leo and VY CMa, as described in Royer et al. (2010) and Decin et al. (2010a). For IK Tau, CW Leo and VY CMa a third-order B3A observation was also available. The B3A band covers approximately the same wavelength range as the B2A band, but surpasses the latter regarding spectral resolution. The second-order B2A band, however, possesses better continuum sensitivity. Therefore, the B2A and B3A bands are both added to the final data sample. The MESS programme also observed SPIRE FTS for 9 of the 24 selected targets and also for AGB target R Scl, which was not observed by the PACS spectrometer. The GT programme of PI Barlow (Barlow 2011) provided SPIRE FTS observations for another 8 of these 24 targets as this programme was specifically proposed to obtain the complementary SPIRE data for some remaining MESS targets.

No HSA PACS-SED spectroscopy products were found for OH 127.8 +0.0. However, Lombaert et al. (2013) presented a complete PACS spectrum of this target, which was observed during calibration time and needed alternative data reduction. Their final data product was added to the data sample.

Complementary SPIRE FTS data for OH 127.8 +0.0 was obtained by the Open Time (OT) programme of PI Justtanont (Justtanont 2011) as well as standard mode PACS and SPIRE spectroscopic data for five more targets. Their programme concentrated on studying the chemistry, cooling, and geometry of the circumstellar environment of M-type stars with very strong MLRs. Some other AGB targets were included in the *Herschel* filler programme (OBSSHerchel1) which observed six complete PACS spectra (B2A + short R1 and B2B + long R1) and additional SPIRE FTS for two of these targets. Finally, incomplete PACS spectra (only the B2A + short R1 band) were obtained for RR Aql during OBSSHerchel1, and for T Cep and R Aql within the OT programme of Cami (2011).

Spectroscopic data could also be retrieved for the AGB stars OH 30.7 +0.4 (Justtanont 2011), ST Her, G Her, V438 Oph (Cami 2011) and RT Cap and AQ Sgr (OBSSHerchel1).

However, these targets were not included in the final data selection because of an insufficient signal-to-noise ratio (S/N).

PACS and SPIRE photometry could additionally be obtained for most of the sample targets. The MESS programme contains corresponding PACS (blue + red) scan maps for all MESS and OBSSHerchel1 spectra, except for IRAS 09425–6040, AFGL 5379, AFGL 2513 and GY Aql, and it also has SPIRE large maps for half of these targets. Supplementary PACS green band scan maps are found for TX Cam, LL Peg, R Cas, α Ori (Royer 2011) and for EP Aqr (Cox 2011). Photometry taken in PACS-SPIRE parallel mode within the *Hi-GAL* programme (Molinari 2007, 2010; Molinari et al. 2010, 2016) produced large-area scan maps of the galactic plane region, containing another eight of our sample targets. Photometry for T Cep was obtained by André (2007), also in PACS-SPIRE parallel mode.

2.2. Data processing

2.2.1. PACS spectroscopy

All data was reduced with the standard interactive pipeline in HIPE (Ott 2010), version 14.1 in combination with version 78 of the calibration tree. The flux calibration (which includes spatial flat-fielding) is performed via normalisation to the telescope background. The final re-binning is performed with an oversampling of two, thus with Nyquist sampling with respect to the instrumental resolution. The spectra were extracted assuming a point source approximation and a point source correction was applied for every target. This point source correction is wavelength dependent so that the spectral fluxes are to be understood as measured in an infinite aperture.

AGB stars with especially heavy mass loss are not perfect point sources. However they never fill the beam as assumed in the extended source calibration. Only CW Leo is extended beyond the 3×3 central spaxels that are used to derive the total flux (see below).

For most of the targets, the spectrum was extracted from the central spaxel (hereafter c1) and subsequently scaled by the flux level of the summed spectrum of the 3×3 central spaxels (c9), resulting in a spectrum which accounts for the flux lost from the central spaxel. An exception is TX Cam which shows high flux values in the surrounding spaxels compared to c1. In this case the summed spectrum in the 3×3 central spaxel box was taken, with the c9-to-total point source correction applied. In case of OH 30.1 –0.7 and OH 32.8 –0.3 the c1-spectrum without subsequent scaling was preferred because inhomogeneous background emission affects the scaling to c9. The choice of c1 is also justified by the fact that very little flux (<10%) is found in the surrounding spaxel with respect to the central one, hence rendering the flux correction too uncertain.

The observations for AFGL 5379 and OH 21.5 +0.5 suffered from mispointing by about $18''$. In these cases, the spectrum was extracted from the spaxel containing the actual source, and applying the proper point source correction for a single spaxel. These sources and the others discussed below which showed some problems or needed some alternative treatment are flagged in Table A.1.

The standard pipeline eliminates the noisiest parts of the spectra and the regions affected by light leaks, and the wavelength ranges of the spectral bands are confined to: B2A segments between 55 and 72 μm , B3A segments between 55 and 70 μm , B2B segments between 70 and 95 μm and R1 segments between 102 and 190 μm .

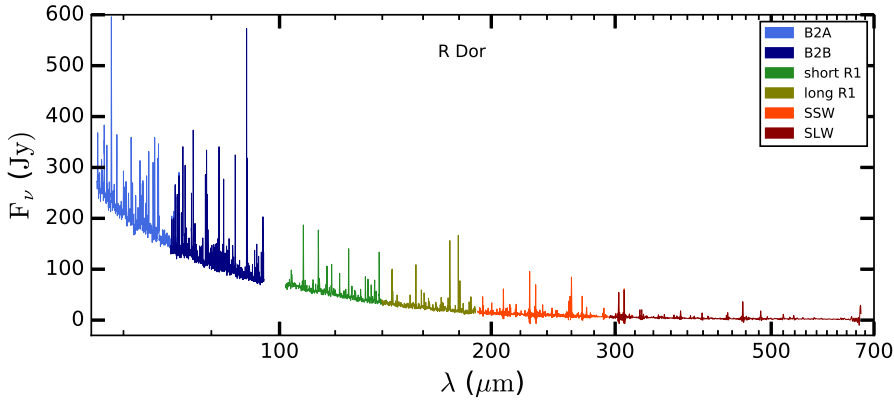


Fig. 1. Full-range PACS and SPIRE spectra for R Dor. The PACS spectrum consists of bands B2A (55–72 μm), B2B (70–95 μm), short R1 (102–146 μm) and long R1 (140–190 μm). The SPIRE spectrum is made up from the SSW (191–317 μm) and SLW band (294–670 μm). The spectra of all stars in the sample are available at the CDS.

The spectra for all targets and all individual spectral bands are available in ASCII format at the CDS. These files contain wavelength, flux, and flux uncertainty. The flux uncertainty results from the production of the final spectrum. The wavelength bins of the final spectrum are composed of multiple data points which are obtained in the different detectors and during different positions of the grating. These single spectra are averaged and the corresponding standard deviation of the data is a good measure for the scatter in the flux level. According to the PACS observers manual the relative flux calibration accuracy within a PACS band is 10% (20% in R1), while the absolute flux calibration error is $\sim 12\%$ across the entire wavelength range⁴.

2.2.2. SPIRE spectroscopy

The HIPE pipeline version 14.1 and the latest set of calibration files of version 14.3 were used to reprocess the SPIRE FTS data. Assuming that all targets were point sources or only slightly extended sources at SPIRE spatial resolution, only the central detector feed horns of the SSW and the SLW bolometer arrays were reduced.

The standard pipeline subtracts the telescope background emission, which generally approximates the real background spectrum to within 1%. Strong far-IR emission from the Galactic plane, however, heavily affected the calibration of OH 127.8 +0.0, TX Cam, II Lup, AFGL 5379, OH 21.5 +0.5, OH 26.5 +0.6, OH 30.1 –0.7, IRAS 18488–0107, OH 32.8 –0.3, and IRAS 19067+0811. The extra background contamination lead to a discontinuity between the SSW and SLW band in the reprocessed spectrum. To correct for this, we performed an additional background subtraction, following the method described in the *SPIRE Data Reduction Guide*⁵. In this method, the averaged off-axis detectors are subtracted from the central detector. The low-frequency information was extracted from the off-axis spectra by smoothing them with a wide kernel. An illustration of this kind of contamination and a detailed description of the corresponding background subtraction is given in Appendix B for OH 30.1 –0.7.

All spectra are kept unapodised to preserve the original, sinc-function line profiles with a spectral resolution of 1.4 GHz (FWHM). The SSW and SLW spectra are available in ASCII format at the CDS. These files contain wavelength, flux, and flux uncertainty, which is the standard deviation of the averaging process of the data points from the different detectors and observation scans. The SPIRE handbook states that there is a possible

continuum offset error of 0.4 Jy for SLW and 0.3 Jy for SSW, and a calibration error of 6%.

An example of a combined full-range PACS and SPIRE spectrum is shown in Fig. 1 for the M-type AGB-star R Dor.

2.2.3. PACS and SPIRE imaging

The latest PACS level 2.5 scan maps were downloaded from the HSA. The data are the final legacy products generated in an automated fashion by the *Herschel* Standard Product Generator pipelines, using HIPE version 14.2 of the software. We used the maps generated by the JScanam pipeline, obtained by combining the orthogonal scan and cross-scan AORs.

The SPIRE large maps are the best science quality level 2 products created with version 14.1 of HIPE that were obtained from the HSA for all bands and for both the point source and the extended source calibration.

Scan maps in PACS-SPIRE parallel mode of level 2 and 2.5 were also downloaded from the HSA. The maps were obtained by two orthogonal scans, adopting the default fast scan velocity of $60'' \text{ s}^{-1}$ and they were created by the HIPE 14.2 and 14.1 software version for PACS and SPIRE wavelengths, respectively.

3. Quality check of the flux calibration

In order to check the calibration quality of the spectra, the flux level is compared to the source flux measured in the photometer maps. As the spectra were extracted by assuming point source targets (see Sect. 2.2), the imaged photometry was derived following a point source assumption for consistency. The details on the methods used to obtain the source photometry fluxes are given in Sect. 3.1.

The flux measured in the imaged maps depends on the spectral shape of the source spectrum and the response of the overall instrumental setup, while on the other hand, the spectral fluxes can be considered to be monochromatic. To compare the flux measured by the bolometers to that of the spectra, the *synthetic photometry* was calculated by convolving the flux spectra with the response functions of the photometric system, as explained in Sect. 3.2. The obtained photometric source fluxes and the derived synthetic fluxes can then directly be compared to each other. The results of this comparison are given in Sect. 3.3.

3.1. Imaged source photometry

PACS source photometry was carried out by performing aperture photometry using the *annularSkyAperturePhotometry* task

⁴ See Sect. 4.10 in the PACS observers manual.

⁵ http://herschel.esac.esa.int/hcss-doc-13.0/load/spire_drg/html/spire_drg.html

that comes with HIPE. The recommended⁶ source and background apertures for point sources were adopted (Table 3) and the *daophot* option was chosen to estimate the sky background. Subsequently, a point source correction was performed by the HIPE *photApertureCorrectionPointSource* task. The method gave unreliable results for OH 21.5 +0.5, OH 30.1 –0.7, IRAS 18488–0107, OH 32.8 –0.3, and IRAS 19067–0811 due to their weak brightness and the strong galactic background emission. For these sources a source aperture which visually contained all source flux was applied and a representative surrounding annulus was chosen as background aperture.

The recommended method to obtain SPIRE point source photometry is to perform fitting of the timeline data. This method fits source and background simultaneously in the level 1 timeline data products and was adopted for most of our sources. The sources OH 21.5 +0.5, IRAS 18488-0107, OH 32.8 –0.3, and IRAS 19067–0811 were too weak at SPIRE wavelengths to derive a reliable photometric flux in any of the SPIRE bands, while OH30.1 –0.7 was only sufficiently bright in the 250 μm band. The timeline fitting also failed to produce reliable results for R Scl and R Aql as the best-fit PSF exceeded the confidence limits. In these two cases, aperture photometry (HIPE DaoPhot task) was instead carried out on the maps calibrated for extended emission for all SPIRE bands of R Scl and for the 250 μm and 350 μm bands of R Aql.

The results for the source photometry can be found in Table 4. We repeat that all photometry is derived by using apertures optimised for point sources, and then applying a point source correction. For targets showing extended circumstellar emission, the flux values can therefore be lower than those derived with source apertures that include this extended emission. Likewise, they can also significantly differ from lower spatial resolution literature photometry that does not resolve the extended emission. The sample targets with a significant contribution from extended emission are: CW Leo, α Ori, *o* Cet, W Hya, X Her, R Cas, R Scl and V1943 Sgr.

No colour correction was applied to the derived values. The reader can find values for the colour corrections in the instruments manuals, and they are also available in the HIPE calibration files. They are a few percent at both PACS (Poglitsch et al. 2010) and SPIRE wavelengths (SPIRE handbook) for energy distributions typical of late-type stars.

3.2. Synthetic photometry from the spectra

SPIRE synthetic photometry was obtained by use of the built-in *spireSynthPhotometry* task in HIPE. This task uses the SPIRE photometer relative spectral response functions (RSRFs) available in the calibration files to calculate the synthetic photometry at the overlapping photometer wavelength bands by weighting the spectrum with the RSRFs of the different bands.

A similar method was carried out for PACS. The RSRFs of the PACS photometer bands are closely approximated by combining the different filter transmission curves and the PACS bolometer response curve which are both available in the HIPE calibration files. To fully cover the green band, the gap in the spectrum between the B2B and R1A segment was bridged by a power law function $F_\lambda = a\lambda^{-b}$ which best fitted the spectrum between 80 and 120 μm . Also, the PACS spectrum was extended to longer wavelengths as the red photometric band exceeds the

Table 3. Source apertures and sky background annuli used to obtain PACS source photometry.

Name	Band	Source annulus (")	Sky ($R_{\text{inner}}, R_{\text{outer}}$) annulus (", ")
<i>Recommended</i>	Blue	12	(35, 45)
	Green	12	(35, 45)
	Red	22	(35, 45)
OH 21.5 +0.5	Blue	40	(40, 60)
	Red	15	(40, 60)
OH 30.1 –0.7	Blue	40	(40, 60)
	Red	25	(40, 60)
IRAS 18488–0107	Blue	40	(40, 60)
	Red	15	(40, 60)
OH 32.8 –0.3	Blue	25	(25, 30)
	Red	25	(25, 40)
IRAS 19067+0811	Blue	30	(40, 60)
	Red	10	(20, 25)

Notes. Source apertures and sky background annuli used for the HIPE *annularSkyAperturePhotometry* task to obtain PACS source photometry. The recommended apertures are adopted for all sources, except for the ones that are explicitly listed.

190 μm wavelength limit in the spectrometer. When a SPIRE spectrum is available, both PACS and SPIRE spectra are combined to cover the full wavelength range of the red band. When no SPIRE spectrum is available, the long R1 segment of the spectrum is extrapolated to longer wavelengths (320 μm) using a power law function $F_\lambda = a\lambda^{-b}$ which best fitted the spectrum between 130 and 180 μm . As a second step, the integrated fluxes are divided by the width of the bands to obtain a monochromatic flux $F_{\lambda_{\text{eff}}}$ at the effective wavelength of each band: $F_{\lambda_{\text{eff}}} = \frac{\int F_\lambda d\lambda}{\Delta_\lambda}$. The reasoning behind this and the values for the band widths and the effective wavelengths are listed in the PACS Technical note PICC-CR-TN-044, issue 1.1⁷.

3.3. Imaged vs. synthetic photometry

The results of the comparison between imaged and synthetic photometry are summarised in Table 4. No imaged PACS or SPIRE photometry is available for IRAS 09425–6040, AFGL 2513, RR Aql and GY Aql. On the other hand, no synthetic photometry could be derived for T Cep, R Aql and RR Aql as these spectra lack the B2B and long R1 segments. For most of the targets, synthetic and imaged photometry are in agreement within the mutual 15% uncertainty level. The targets for which a significant difference is found between imaged and synthetic fluxes in at least one colour are flagged with a † symbol and the corresponding flux values are indicated in bold. These sources are also flagged in Table A.1. For these targets it is recommended that the PACS and SPIRE spectra, as well as the imaging, be treated with care.

Except for the difference between SLW and PSW fluxes for R Scl (and where the flux is very low anyway) none of the larger differences is in a source where extended emission might play a role in the derivation and comparison of fluxes derived from the spectra and the imaging.

⁶ https://nhscsci.ipac.caltech.edu/workshop/Workshop_Oct2014/Photometry/PACS/PACS_phot_Oct2014_photometry.pdf

⁷ <http://herschel.esac.esa.int/twiki/pub/Public/PacsCalibrationWeb/PICC-CR-TN-044.pdf>

Table 4. Synthetic photometry from the spectra compared to imaged photometry.

Identifier	PACS sp.	PACS im.	PACS sp.	PACS im.	PACS sp.	PACS im.	PACS sp.	PACS im.	PACS sp.	PACS im.	SPIRE im.	SPIRE sp.	SPIRE im.	SPIRE sp.	SPIRE im.	SPIRE sp.
	F_{70} (Jy)	F_{70} (Jy)	F_{100} (Jy)	F_{100} (Jy)	F_{160} (Jy)	F_{160} (Jy)	F_{250} (Jy)	F_{250} (Jy)	F_{350} (Jy)	F_{350} (Jy)	F_{350} (Jy)	F_{500} (Jy)				
<i>AGB-stars</i>																
WX Psc†	150.	94.6	64.3	...	18.3	15.2	3.5	...	0.84	...	0.52	0.52
R Scl†	...	17.5	5.7	0.98	...	0.87	...	0.62	0.62	...	0.30
OH 127.8+0.0	87.5	86.9	33.9	...	8.9	10.3	2.21	...	2.0	...	0.66	0.17
<i>o</i> Cet	143.	158.	62.6	...	20.2	23.0	7.5	...	7.04	...	3.6	1.9	...	1.6
IK Tau†	169	167.	70.0	60.5	19.2	21.6	3.8	...	5.1	...	1.9	0.83	...	0.95
R Dor	159	154	76.6	...	27.1	29.3	11.5	...	11.6	...	5.6	3.1	...	2.8
TX Cam	63.3	61.1	27.6	24.8	9.2	8.8	1.65	1.1	0.51
09425-6040	14.1	...	6.6	...	2.1
CW Leo	2461.	2367.	985.	850.	280.	334.	74.5	...	64.9	...	41.2	17.7	...	16.
RW Lmi	157.	142.	71.3	...	23.3	24.6	7.4	...	6.6	...	4.0	2.1	...	1.6
V Hya	60.6	58.0	28.2	...	9.4	9.9	2.8	...	2.8	...	1.6	0.79	...	0.69
W Hya	107.	119.	53.1	...	22.3	23.0	8.4	...	8.5	...	3.8	2.1	...	2.0
II Lup†	66.5	89.5	31.9	...	11.3	15.9	3.8	1.8	0.96
X Her	16.6	17.1	8.1	...	2.9	3.1
AFGL 5379	661.	633.	271.	...	64.1	79.3	20.5	5.8	1.7
OH 21.5+0.5†	123.	36.3	45.3	...	9.7	6.0	1.3	...	0.06	-0.3
OH 26.5+0.6	323.	323.	143	...	35.9	36.7	7.4	...	8.4	...	1.1	0.02	...	0.64
OH 30.1-0.7	133.	148.	59.3	...	16.0	15.5	4.0	...	4.0	...	-0.12	-0.35
18488-0107†	33.8	17.8	15.2	...	5.6	3.0	2.2	0.9	0.19
OH 32.8-0.3†	116.	56.3	43.4	...	11.6	7.0	3.8	0.05	-0.20
R Aql	...	23.7	4.8	1.58
19067+0811	21.6	24.1	8.6	...	1.8	2.1	0.86	-0.31	-0.47
W Aql	41.2	46.7	19.1	...	6.0	7.8
GY Aql	31.2	...	13.3	...	4.3
χ Cyg	42.6	42.7	19.4	...	6.4	7.6
V 1943 Sgr	13.1	12.8	6.0	...	2.2	2.4	1.1	0.37	0.11
AFGL 2513	15.5	...	7.6	...	2.9
IRC -10 529†	109.	72.4	47.0	...	13.2	11.1	2.9	1.2	0.42
T Mic	15.7	15.8	6.63	...	2.6	3.0
V Cyg	25.4	23.9	12.0	...	4.2	5.0
T Cep	...	19.8	4.0
EP Aqr	23.4	22.3	10.5	10.0	3.8	3.7
π Gru	31.0	33.1	13.8	...	5.0	5.4	1.6	0.39
LL Peg	174.	173.	82.4	79.9	27.0	27.3	6.0	...	7.7	...	3.1	1.4	...	1.3
LP And	82.0	63.6	36.8	...	11.7	10.9
R Cas	52.0	55.5	24.6	22.3	8.4	10.0	3.3	...	3.2	...	1.6	1.0	...	0.76
<i>Red Super Giants</i>																
α Ori†	127.	129.	57.1	53.6	18.1	20.7	4.5	...	6.5	...	2.7	1.4	...	1.7
VY CMa	1125.	1083.	454.	...	132.	148.	41.6	16.7	7.1
NML Cyg	707.	726.	339.	...	108.	119.	37.1	18.4	8.2

Notes. Synthetic photometry from the spectra (PACS/SPIRE sp.) is compared to imaged photometry (PACS/SPIRE im.). Values not in agreement within the respective 15% error levels (that is, differ by more than 30%) are indicated in **bold** and the corresponding targets are flagged with a †.

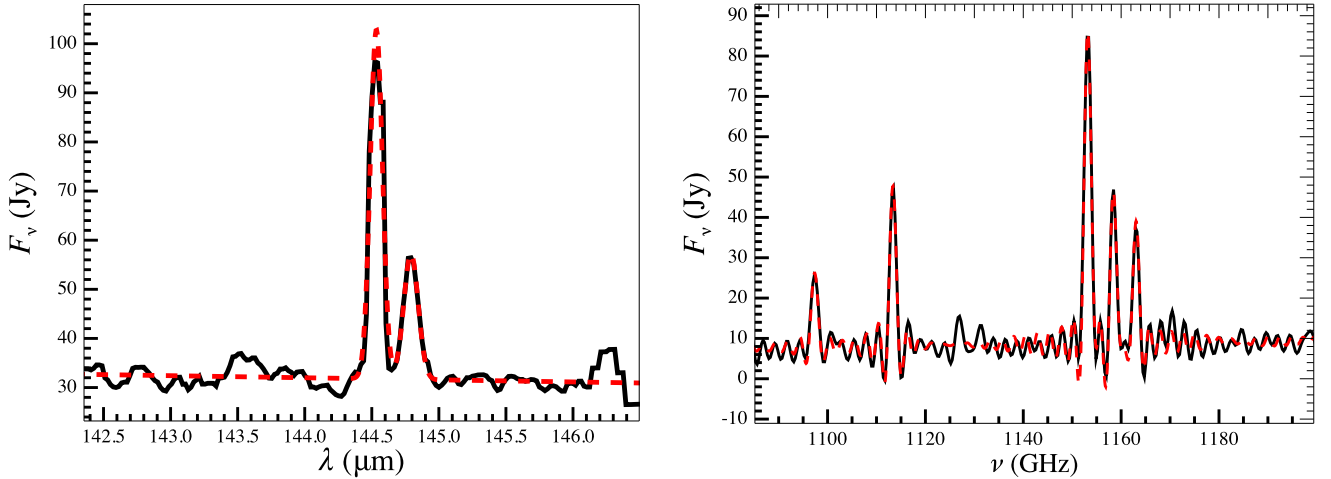


Fig. 2. Example of line fitting (red dotted line) for the PACS and SPIRE spectrum (black full line) of the M-type AGB-star R Dor. The fitting functions are Gaussians for PACS (*left panel*) and sinc functions for SPIRE (*right panel*). The local maxima at 143.5 and 146.2 μm and 1130 GHz have not been selected as lines by the algorithm.

Essentially all of our targets are variable, and many belong to the Mira class showing the largest variations. As the imaging and spectra are not taken at the same time, differences in flux levels between the two could be due to variability. However, there is not enough data available to be more specific. Only CW Leo has been observed over its pulsation cycle (Groenewegen et al. 2012) indicating peak-to-peak variations of about 25%, 23%, and 21% in the PSW, PMW and PLW filters, respectively, or about 0.2 mag. At PACS wavelengths it has not been measured, but we expect the variations to be larger. For comparison, the peak-to-peak amplitude in the K -band for CW Leo is 2.0 mag (Le Bertre 1992).

4. Data analysis

4.1. Line detection and measurement

The selection and measuring of the spectral lines was performed following a general and consistent algorithm for all targets. This algorithm differed slightly for PACS and SPIRE spectra, since the SPIRE instrument is a Fourier transform spectrometer, providing sinc-shaped spectral profiles.

In the case of PACS, all local maxima were first detected in the spectrum. From this pre-selection, only the maxima meeting the following two conditions made it to the final list of spectral lines: (1) they must be separated by at least one full width at half maximum (FWHM) to ensure that they can be distinguished from neighbouring spectral lines and (2) the flux density corresponding to the wavelength of the local maximum must be sufficiently high relative to the local noise level in order to minimise the selection of spurious lines. After extensive testing, $F_{\lambda_{\text{max}}} \geq 4.25 \times \text{MAD}_{36\text{FWHM}}$ was adopted as a criterion, where the median absolute deviation (MAD) was calculated locally for a wavelength region spanning 36 FWHM around the local maximum in question. This corresponds to 0.015–0.021 μm in B3A, 0.034–0.039 μm in B2A and B2B, and 0.11–0.13 μm in R1 around each peak. The MAD was used instead of a traditional root mean square to measure the noise level as it is more stable to outliers. The flux level criterion and the width of the wavelength region used in the procedure were determined by running the algorithm looking for “negative lines” and then minimising the detection of actual noise peaks as true lines.

Table 5. Input molecular species and abundances relative to H_2 (in exponential notation) adopted for the identification of the spectral lines.

Species	$n(X)/n(\text{H}_2)$					
	M-type	Ref.	S-type	Ref.	C-type	Ref.
CO	3.0 (–4)	1,2	6.0 (–4)	3,4	1.0 (–3)	2
^{13}CO	2.3 (–5)		2.4 (–5)		3.0 (–5)	
C^{17}O	3.0 (–7)		6.0 (–7)		1.0 (–6)	
C^{18}O	3.0 (–7)		6.0 (–7)		1.0 (–6)	
H_2O	1.0 (–4)	5	1.0 (–5)	2	1.0 (–5)	6
H_2^{17}O	1.0 (–7)		1.0 (–8)		1.0 (–8)	
H_2^{18}O	1.0 (–7)		1.0 (–8)		1.0 (–8)	
SiO	6.0 (–6)	7	6.0 (–6)	8	1.0 (–6)	9
^{29}SiO	3.0 (–7)		3.0 (–7)		5.0 (–8)	
^{30}SiO	2.0 (–7)		2.0 (–7)		3.3 (–8)	
SO	3.5 (–6)	10,11,12	3.5 (–6)		...	
SO ₂	2.5 (–6)	10,11,12	2.5 (–6)		...	
SiS	3.0 (–7)	13	8.0 (–7)		3.0 (–6)	13
^{29}SiS	1.5 (–8)		4.0 (–8)		1.5 (–7)	
^{30}SiS	1.0 (–8)		2.7 (–8)		1.0 (–7)	
HCN	1.2 (–7)	14	7.0 (–7)	14	2.9 (–5)	14
H^{13}CN	9.2 (–9)		2.8 (–8)		8.5 (–7)	
PO	1.0 (–7)	15	1.0 (–7)		...	
PN	1.0 (–7)	15	1.0 (–7)		...	
CS	1.0 (–7)	10,12,16	5.0 (–7)		1.0 (–6)	17,18,19
^{13}CS	7.7 (–9)		2.0 (–8)		3.0 (–8)	
CN	1.0 (–7)	10,12,16	1.0 (–5)	3,4	2.0 (–5)	18,19
^{13}CN	3.9 (–9)		4.0 (–7)		5.9 (–7)	
NH_3	7.5 (–7)	20	7.5 (–7)		7.5 (–7)	
H_2S	1.0 (–8)	21	1.0 (–8)		4.0 (–9)	17
C_2H_2		1.0 (–5)	22
CCH		5.0 (–6)	18
C_4H		3.0 (–6)	18,19
HC_3N		1.0 (–6)	18,19
SiC_2		2.0 (–7)	18,19,23
$^{29}\text{SiC}_2$		1.0 (–8)	
$^{30}\text{SiC}_2$		6.7 (–9)	

References. (1) Ziurys et al. (2009), (2) Danilovich et al. (2015), (3) Danilovich et al. (2014), (4) Schöier et al. (2011), (5) Maercker et al. (2016), (6) Lombaert et al. (2016), (7) González Delgado et al. (2003), (8) Ramstedt et al. (2009), (9) Schöier et al. (2006), (10) Decin et al. (2010b), (11) Danilovich et al. (2016), (12) Velilla Prieto et al. (2017), (13) Schöier et al. (2007), (14) Schöier et al. (2013), (15) De Beck et al. (2013), (16) Kim et al. (2010), (17) Agúndez et al. (2012), (18) Zhang et al. (2009), (19) Woods et al. (2003), (20) Wong et al. (2015), (21) Gobrecht et al. (2016), (22) Fonfria et al. (2008), (23) Cernicharo et al. (2010). References for the isotopic ratios are listed in the main text.

Table 6. Rotational temperatures.

Name	CO		HCN	
	$T_{\text{rot,cool}} (\sigma_{T,c})$ (K)	$T_{\text{rot,hot}} (\sigma_{T,h})$ (K)	$T_{\text{rot,cool}} (\sigma_{T,c})$ (K)	$T_{\text{rot,hot}} (\sigma_{T,h})$ (K)
WX Psc	93 (13)	481 (53)
R Scl	56 (12)
OH 127.8 +0.0	...	939 (33)
<i>o</i> Cet	94 (8)	520 (155)
IK Tau	96 (11)	463 (39)
R Dor	99 (11)	524 (46)
TX Cam	80 (7)	396 (55)
IRAS 09425–6040	...	365 (202)
CW Leo	109 (10)	692 (22)	119 (12)	753 (34)
RW LMi	101 (9)	642 (27)	118 (13)	662 (35)
V Hya	99 (10)	696 (25)	142 (13)	667 (29)
W Hya	112 (9)	460 (111)
II Lup	99 (10)	449 (18)	118 (13)	452 (19)
X Her	...	1722 (314)
AFGL 5379	94 (10)	768 (511)
OH 26.5 +0.6	88 (16)	582 (75)
OH 30.1 –0.7	58 (11)
IRAS 18488–0107	41 (6)	785 (168)
OH 32.8 –0.3	15 (1)
W Aql	...	527 (14)
GY Aql	...	363 (36)
χ Cyg	...	641 (28)
V1943 Sgr	72 (6)	743 (105)
AFGL 2513	...	608 (27)	...	668 (37)
IRC –10 529	132 (10)	471 (54)
T Mic	...	458 (53)
V Cyg	...	564 (24)	...	462 (38)
T Cep	...	568 (155)
EP Aqr	...	911 (235)
π Gru	...	668 (27)
LL Peg	92 (8)	459 (30)	115 (7)	484 (38)
LP And	109 (9)	606 (21)	125 (13)	650 (30)
R Cas	92 (9)	455 (50)
α Ori	96 (8)	681 (41)
VY CMa	119 (7)	471 (32)
NML Cyg	100 (10)	528 (36)

Notes. Rotational temperatures, either a single value or separated into a cool and hot component. Error bars are given between parenthesis.

Subsequent to the line selection, the integrated fluxes were measured by fitting a Gaussian to the line profile, while locally approximating the continuum by a first-order polynomial. Neighbouring lines were fitted together when this improved the goodness of the fit and to account for line blends. The quality of the fits was manually checked, resulting in a removal of less than 10% of the lines which were judged unsatisfactory. An illustration of such a fit with multiple lines in the PACS range of R Dor is given in the left panel of Fig. 2.

In case of SPIRE, spectral lines were selected and measured in an iterative way. During each iteration step, the strongest local maximum that satisfied the following two conditions, was selected as a spectral line: (1) they must be separated by at least one FWHM from spectral lines detected during previous iterations and (2) $F_{\lambda_{\text{max}}} \geq 8.0 \times \text{MAD}_{36\text{FWHM}}$. The stricter criterion is justified as the Fourier transform nature and the lower resolution of the spectra make the line-noise distinction harder and was derived by minimising the detection

of false lines when running the algorithm on negative noise peaks.

After a line is selected, the integrated flux is measured by simultaneously fitting the spectral line in question, together with the continuum and the lines selected during all previous iteration steps. The fitted model consisted of a fifth-order polynomial, which approximates the continuum, plus a sinc function for each line. The residual spectrum then served as input for the next iteration step. The algorithm continued until no more lines were found that satisfied the conditions as described above. The right panel of Fig. 2 shows an example of line fitting in the SPIRE range of R Dor.

The detected lines and the derived line fluxes are reported for each target in Appendix E. The reported total uncertainty represents the fitting uncertainty. Line identifications are discussed in Sect. 4.2 and are reported in Appendix E.

The line sensitivity varies from source to source as the number of repetitions of a line scan (for PACS) or spectral

map (for SPIRE) varies. The best line sensitivities achieved in some sources are $8.4 \times 10^{-18} \text{ W m}^{-2}$ (in the 65–72 μm range in B2A), $6.3 \times 10^{-18} \text{ W m}^{-2}$ (in the 75–94 μm range in B2B), $3.6 \times 10^{-18} \text{ W m}^{-2}$ (in the 120–140 μm range in R1 short), $2.9 \times 10^{-18} \text{ W m}^{-2}$ (in the 140–190 μm range in R1 long), $1.9 \times 10^{-18} \text{ W m}^{-2}$ (in the 270–300 μm range in SSW), $1.5 \times 10^{-18} \text{ W m}^{-2}$ (in the 300–450 μm range in SLW), while the typical sensitivities are a factor of 3 (SPIRE) and 4–6 (PACS) worse.

4.2. Line identification

The resulting line lists were cross-referenced to the molecular spectroscopic catalogues of the CDMS⁸ and JPL⁹ databases in order to identify the corresponding chemical species. For each observed spectral line, molecular transitions are searched for within a wavelength region of half the FWHM around the observed central wavelength. The spectral lines were all corrected for the velocity of the local standard of rest (v_{LSR}) which are listed in Table 2.

As multiple transitions of different chemical species could belong to a specific spectral line, an abundance analysis assuming local thermodynamic equilibrium (LTE) was performed to indicate the most probable contributors. In LTE, the level populations n_i are given by

$$\frac{n_i}{n} = g_i \frac{e^{-E_i/k_b T}}{Q(T)},$$

with n the total abundance of the species, g_i the degeneracy and E_i the energy of state level i , T the excitation temperature of the particles, and $Q(T)$ the partition function of the species. The level populations corresponding to all possible molecular transitions for each spectral line were calculated. In the case of optically thin emission the line intensity is proportional to the number density and the Einstein A coefficient of the transition. The relative contribution of each transition of the different chemical species to the observed spectral line could thus be estimated.

The level transitions and molecule-specific properties like statistical weights, transition energies and partition functions were taken directly from the CDMS and JPL catalogues. Additional partition functions for H₂O and C₂H₂ were found in Chen et al. (2000) and Amyay et al. (2011), respectively. The molecules that were considered for the identification are listed in Table 5, together with their typical fractional abundances as found in the literature. The species SO, SO₂, PO and PN were only considered for M- and S-type stars as they either have very low abundances or are undetected in C-type stars. In the same way, the carbon-rich species C₂H₂, CCH, C₄H, HC₃N, SiC₂, ²⁹SiC₂, and ³⁰SiC₂ are only used for the line identification in C-type stars.

The ¹³C isotopologues of CO, HCN, CS and CN are also considered. Typical ¹²C/¹³C ratios of 13, 25 and 34 for respectively M-type, S-type and C-type stars are adopted (Ramstedt & Olofsson 2014).

The ¹⁷O and ¹⁸O isotopologues are only considered for CO and H₂O, as these isotopologues are typically 2–3 orders of magnitude less abundant than the ¹⁶O ones, which would lead to undetectable amounts of isotopologues of other molecules. Previous studies (recently e.g. Hinkle et al. 2016 or De Nutte et al. 2017 and references therein) also show a wide range in ¹⁶O/¹⁷O and

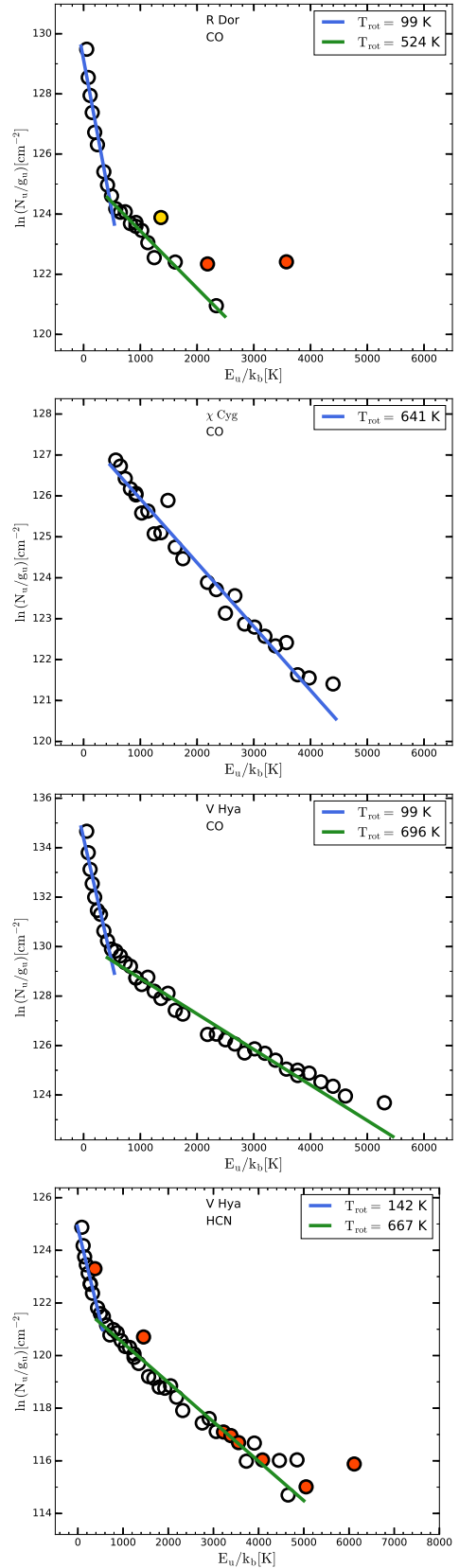


Fig. 3. Examples for rotational diagrams for CO in R Dor and χ Cyg, and CO and HCN in V Hya. The other diagrams are given in Appendix C. Yellow and red symbols are points excluded from the fit (see text for details).

¹⁶O/¹⁸O ratios. For simplicity, an isotopic ratio of 1000 for both ¹⁶O/¹⁷O and ¹⁶O/¹⁸O was chosen.

⁸ The Cologne Database for Molecular Spectroscopy, available at <http://www.astro.uni-koeln.de/cdms>, see Müller et al. (2001).

⁹ Available at <http://spec.jpl.nasa.gov/>, see Pickett et al. (1998).

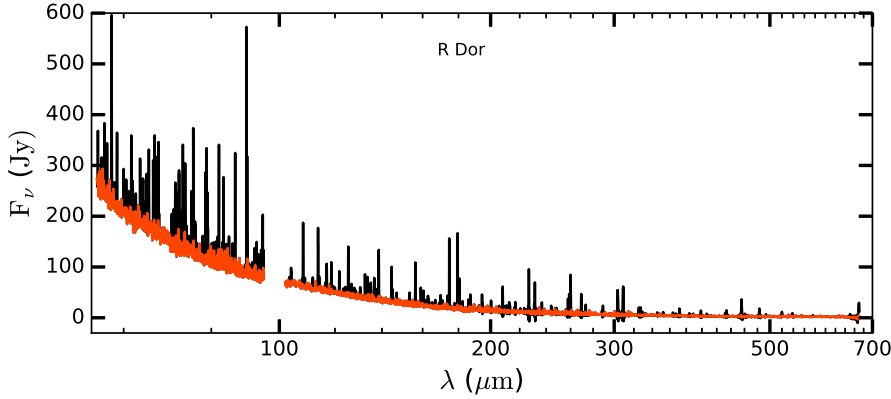


Fig. 4. Derived continuum spectrum (red) of R Dor, extracted from the complete spectrum (black) and removal of all identified spectral lines. In this best estimate of the dust continuum spectrum weaker lines and the effect of imperfect removal of the strongest lines remain visible. The continuum spectra of all stars in the sample are available at the CDS.

Finally, the ^{29}Si and ^{30}Si isotopologues of SiO, SiS, and SiC₂ were also considered. Solar isotopic ratios (Asplund et al. 2009) of 20 and 30 for $^{29}\text{Si}/^{28}\text{Si}$ and $^{30}\text{Si}/^{28}\text{Si}$, respectively are adopted. This is justified as studies of evolved low-mass stars find similar values (e.g. Velilla Prieto et al. 2017; Decin et al. 2010b; Schöier et al. 2011; Danilovich et al. 2014).

The LTE abundance analysis was performed for three different temperatures 75 K, 300 K, and 500 K. In doing so, a large part of the CSE from the warmer inner envelope to the colder outer regions is covered. Also, a biased identification due to a spurious choice of temperature is avoided. The choice of 500 K as the maximum value is justified by the fact that chemical data and properties are often lacking for higher temperatures. For each target, the complete line list with possible identifications for the three temperatures is given in Appendix E. The uncertainty on the identification is dependent on the validity of the LTE assumption, the assumption of optically thin line emission, the adopted abundances and temperatures and on the uncertainties and incompleteness of the data provided in the CDMS and JPL catalogues. An extra uncertainty is added when transitions of isotopologues are involved, as their real isotopic ratios are often highly dependent on the initial mass and the evolutionary status of the target, see e.g. Cristallo et al. (2015), Marigo et al. (2016), Karakas & Lugaro (2016), De Nutte et al. (2017).

Atomic transitions have not been explicitly searched for using the methodology described above. Atomic transitions have not been studied very extensively in AGB stars, although the C I (1–0) line at 609 μm (492 GHz) has been detected in a few AGB stars using heterodyne techniques. In Appendix F we briefly discuss the presence of some well-known atomic lines.

4.3. Rotation diagrams

The rotation diagrams technique was used to estimate the typical excitation temperatures of the circumstellar CO gas for all targets and of HCN for the carbon stars in the sample. These two molecules are the only ones for which there is sufficient multi-transitional data available. Assuming that the spectral lines are optically thin and that the level populations are in local thermal equilibrium (LTE) corresponding to a uniform rotational temperature (T_{rot}) in the gas shell, the following relation holds:

$$\ln \frac{N_u}{g_u} = \ln \frac{N}{Q(T_{\text{rot}})} - \frac{E_u}{k_{\text{B}} T_{\text{rot}}}$$

Here N_u , g_u , and E_u are the population, degeneracy, and excitation energy of the upper level, Q is the partition function of the species and k_{B} is the Boltzmann constant. If sufficient transitions are detected in the PACS and/or SPIRE ranges which cover

Table 7. Power law fits to the different segments of the PACS and SPIRE spectra.

Name	$p(\sigma_p)$	$p(\sigma_p)$	$p(\sigma_p)$
	55–100 μm	100–190 μm	200–670 μm
WX Psc	2.41 (0.01)	2.96 (0.01)	3.44 ^a (0.03)
R Scl	0.71 (0.03)
OH 127.8+0.0	2.38 (0.01)	3.12 (0.02)	3.55 ^a (0.03)
<i>o</i> Cet	2.48 (0.01)	2.57 (0.01)	2.15 (0.01)
IK Tau	2.49 (0.01)	3.15 (0.01)	2.19 (0.02)
R Dor	2.16 (0.01)	2.50 (0.01)	1.97 (0.01)
TX Cam	2.51 (0.01)	2.61 (0.01)	1.99 (0.03)
IRAS 09425–6040	2.02 (0.01)	2.96 (0.01)	...
CW Leo	2.66 (0.01)	2.91 (0.01)	2.43 (0.01)
RW LMi	2.36 (0.01)	2.81 (0.01)	2.18 (0.01)
V Hya	2.32 (0.01)	2.76 (0.01)	2.09 (0.02)
W Hya	1.98 (0.01)	1.83 (0.01)	2.08 (0.01)
II Lup	2.17 (0.01)	2.53 (0.01)	2.19 (0.02)
X Her	2.07 (0.01)	2.48 (0.02)	...
AFGL 5379	2.37 (0.02)	3.83 (0.02)	3.65 ^a (0.01)
OH 121.5+0.5	2.34 (0.01)	3.79 (0.02)	2.43 ^a (0.07)
OH 26.5+0.6	2.70 (0.01)	3.37 (0.01)	3.62 ^a (0.01)
OH 30.1–0.7	2.13 (0.01)	3.07 (0.01)	3.42 ^a (0.02)
IRAS 18488–0107	2.27 (0.01)	2.20 (0.01)	1.27 ^a (0.03)
OH 32.8–0.3	2.69 (0.01)	3.21 (0.01)	3.24 ^a (0.02)
R Aql	1.97 (0.03)	2.47 (0.03)	...
IRAS 19067+0811	2.48 (0.01)	4.41 (0.01)	0.91 ^a (0.06)
W Aql	2.25 (0.01)	3.00 (0.01)	...
GY Aql	2.55 (0.01)	2.76 (0.01)	...
χ Cyg	2.37 (0.01)	2.79 (0.01)	...
RR Aql	2.28 (0.03)	2.58 (0.03)	...
V1943 Sgr	2.37 (0.01)	2.44 (0.01)	2.30 ^a (0.05)
AFGL 2513	2.20 (0.01)	2.41 (0.01)	...
IRC –10 529	2.25 (0.01)	2.79 (0.01)	3.00 (0.02)
T Mic	2.32 (0.01)	2.38 (0.01)	...
V Cyg	2.23 (0.01)	2.74 (0.02)	...
T Cep	2.31 (0.03)	2.45 (0.03)	...
EP Aqr	2.62 (0.01)	2.57 (0.01)	...
π Gru	2.48 (0.01)	2.80 (0.01)	...
LL Peg	2.24 (0.01)	2.60 (0.01)	2.18 (0.01)
LP And	2.39 (0.01)	2.82 (0.01)	2.13 (0.02)
R Cas	2.20 (0.01)	2.67 (0.01)	2.07 (0.02)
α Ori	2.46 (0.01)	2.55 (0.01)	1.68 (0.01)
VY CMa	2.56 (0.01)	2.74 (0.01)	2.68 (0.01)
NML Cyg	2.16 (0.01)	2.66 (0.01)	2.17 (0.01)

Notes. Power law fits to the different segments of the PACS and SPIRE spectra. For each segment the best-fit power index and the 1- σ fitting error (between parenthesis) is given. ^(a)The fitting of the 3rd segment was limited to SSW as the S/N of SLW segment was judged to be too low.

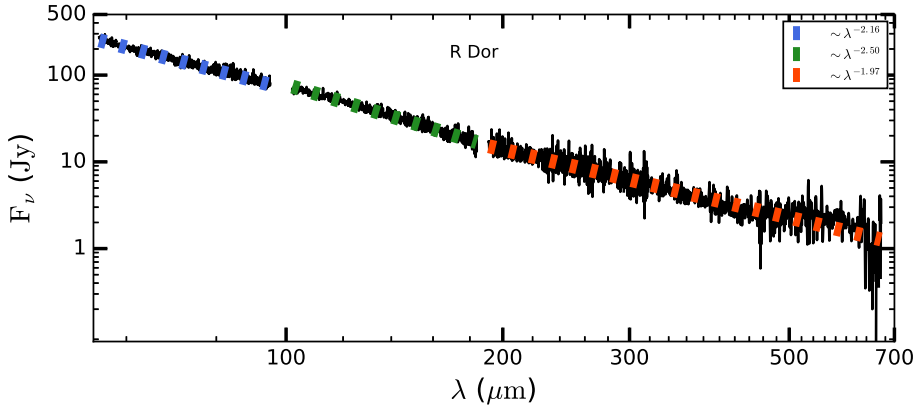


Fig. 5. Example of the power law fit to three segments of a full PACS and SPIRE line-clipped continuum spectrum.

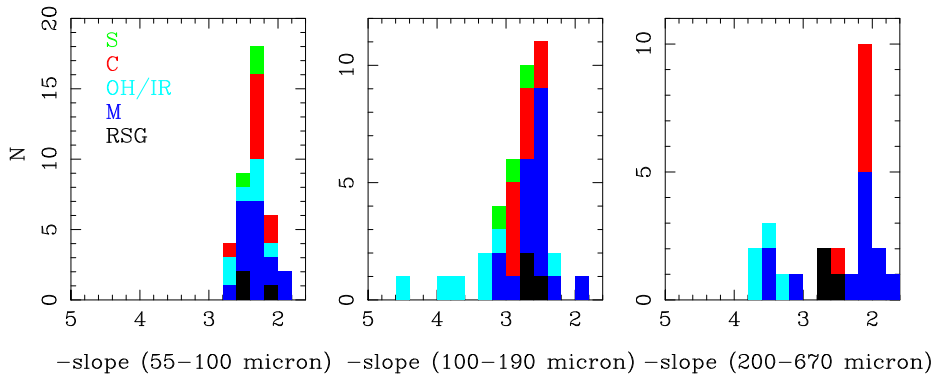


Fig. 6. Histogram of the continuum slopes for the three wavelength regions.

different energy ranges, T_{rot} can be derived by a linear fit of $\ln(N_u/g_u)$ versus $\frac{E_u}{k_B T_{\text{rot}}}$ (see e.g. [Goldsmith & Langer 1999](#), for a didactic outline of this classical method).

Deviations from the above assumptions, like optically thick lines, gas temperatures gradients in the CSE and deviations from LTE will give rise to a non-linear behaviour in the rotation diagrams, meaning that in most cases a single temperature will not describe the data very well. The next simplest approach was adopted by dividing the data into two components when both a PACS and SPIRE spectrum were available. Rotational temperatures were derived by a linear least-squares fit for each of the different components. When at least one of the two components contained fewer than three data points a one-component linear least-squares fit is performed. The fitting is weighted by considering the absolute calibration error and the uncertainty in the line measurement as obtained in Sect. 4.1.

The procedure that was adopted included two iterations steps. Firstly, all lines with a possible contribution from CO or HCN were included in the least-squares fits. This resulted in first estimates for T_{rot} . Secondly, all rotation diagrams were re-fitted, while eliminating the outliers and possible erroneous data points. Data points were traced automatically by considering the relative contribution of the molecule to the spectral line which was calculated for temperatures of 75 K, 300 K, and 500 K as explained in Sect. 4.2 and listed in the tables in Appendix E. The contributions corresponding to the temperature that was closest to the derived T_{rot} from the first iteration step were considered. The CO data points were removed from the fit when their contribution was conservatively estimated to be less than 90% (for HCN a 75% criterion was adopted). In the plots these points were flagged in red. Any remaining obvious outliers were removed manually from the fit and are indicated in yellow in the final plots. The final results are listed in Table 6, while Fig. 3 shows examples of CO rotation diagrams for R Dor, χ Cyg and V Hya, and also the

HCN rotation diagram of the latter target. The rotation diagrams of the other targets can be found in Appendix C. Due to a lack of detected lines, no CO rotation temperature could be derived for OH 21.5 +0.5, IRAS 19067, R Aql, and RR Aql, while no result for HCN could be obtained for R Scl and IRAS 09525-6040. The results are briefly discussed in Sect. 5.3.

4.4. Continuum extraction

The determination of the dust thermal continuum from the complete PACS and SPIRE spectra was done by eliminating the contribution of the detected spectral lines.

The PACS continuum was obtained by replacing each spectral line by the best-fitting first-order polynomial which approximates the local continuum (see Sect. 4.1). Doing this for a wavelength region spanning 3σ around the central wavelength (i.e. $1.27 \cdot FWHM$ of the spectral line), results in a removal of about 99% of the line's contribution.

The contribution of SPIRE spectral lines is contained in the corresponding best-fitting sinc functions as obtained from the algorithm explained in Sect. 4.1. Following the algorithm, the SPIRE continuum was approximated by a fifth-order polynomial. To determine the final estimation of the real SPIRE continuum, this fifth-order polynomial is summed with the residual spectrum of the last iteration step. In this way, information about the spectral noise is preserved and possible quality restrictions of the polynomial fit are eliminated.

As an example, the PACS and SPIRE continuum of R Dor is plotted on top of the original spectrum in Fig. 4. All continua spectra are also available in ASCII format at the CDS.

The spectrum looks noisy especially in the PACS blue range, where the spectral line density is highest. An obvious limitation of the procedure to estimate the continuum is that only the detected spectral lines can be removed. Lines of low intensity are

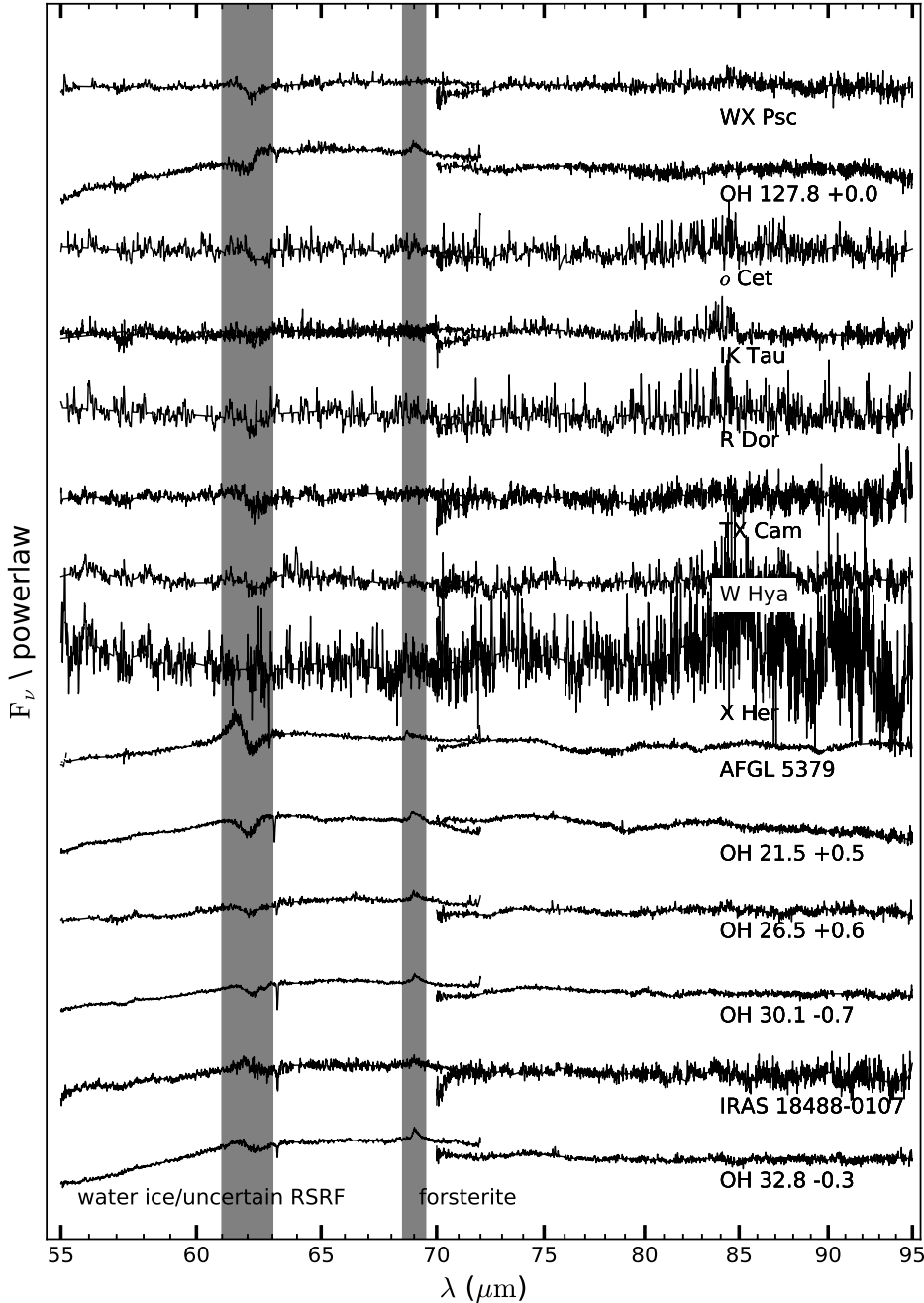


Fig. 7. Continuum divided spectra of M-type targets. The problematic region for the RSRF where the water ice feature is located, and the location of the forsterite feature are indicated.

still present in these spectra. The Gaussian approximation for the shape of the spectral lines and the imperfect removal of the strongest lines may also leave residuals that will be present in these “dust continua” spectra.

4.5. Power law fitting of the dust continuum

Simple power law fitting of the PACS and SPIRE continua is performed to highlight possible differences in dust grain properties and/or in the density structure of the CSEs. The far-infrared and submillimetre energy distribution of evolved stars undergoing mass loss is dominated by thermal emission from dust grains in their CSEs. The dust emission depends on the chemical and morphological properties of the dust grains. Apart from some narrow wavelength bands (a few μm wide) showing some characteristic dust features, these opacities are generally approximated by a power law: $\kappa_\lambda \sim \lambda^{-\beta}$ in the Rayleigh–Jeans regime. In this regime,

thermal black-body emission is characterised by $F_\nu \sim \lambda^{-2}$. When all dust grains have the same temperature, the far infrared energy spectrum can be approximated by a power law: $F_\nu \sim \lambda^{-2-\beta} = \lambda^{-p}$. In reality, dust grain temperatures range from about 1000 K at the dust formation zone to a few tens of Kelvin in the outer regions. At the shortest PACS wavelengths, the emission of the coldest grains could therefore deviate from the Rayleigh–Jeans tail regime. The temperature gradient, in combination with optical depth effect and the morphological structure of the dusty CSE will also deflect the spectra from being a true power law. To account for this, multiple power law fits $\sim \lambda^{-p}$ were used to approximate the PACS and SPIRE spectra. A least-squares fit was performed for the 55–100 μm and 100–190 μm PACS segments separately. The SPIRE continuum as a whole was fitted individually. For some targets only the SSW segment of continuum was considered as the S/N of the SLW segment was considered too low. The fitting is weighted by a combination of the absolute calibration error, the

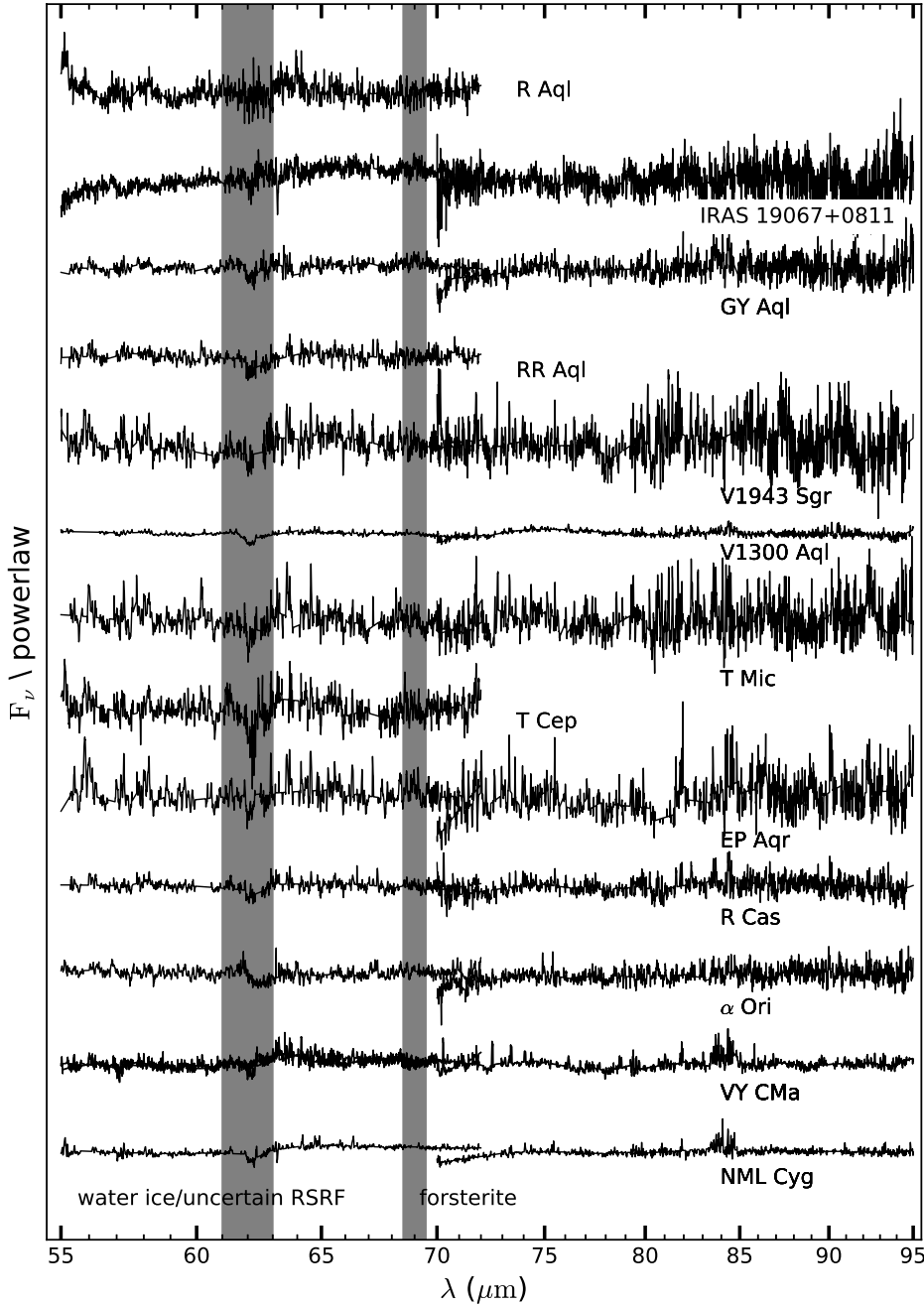


Fig. 7. continued.

standard deviation of the spectra and a possible continuum offset error of 0.4 Jy for SLW and 0.3 Jy for SSW (see Sect. 2.2). The results are listed in Table 7, while Fig. 5 shows an example of the fit for R Dor. The power law fits of the other targets can be found in Appendix D. In some cases there is a mismatch between the PACS and SPIRE spectra and these sources are flagged in Table A.1.

5. Discussion

5.1. Continuum slopes

Figure 6 shows histograms of the continuum slopes based on the data in Table 7. The seven stars with the highest MLRs (in excess of $10^{-4} M_{\odot} \text{yr}^{-1}$) are colour-coded explicitly as OH/IR stars (OH 21.5, OH 26.5, OH 30.1, OH 32.8, and AFGL 5379, IRAS 18448, IRAS 19067, which all three are also known OH

maser sources). The source OH 127.8 is not included in this subsample as its MLR is high but nevertheless a factor of two lower than the lowest MLR of the other seven stars.

In the 55–100 μm region the continuum slopes for M-, S-, and C-stars; OH/IR stars; and RSGs are very similar, roughly between 1.8 and 2.8. What is interesting is that the spread in the slopes is larger in the 100–190 μm region, and that some of the OH/IR stars stand out as having very steep slopes (>3.5), while for the other classes the slope is similar to that at shorter wavelengths. In the SPIRE regime there are fewer stars, and sometimes the slope is only based on the SSW part, but the trend is the same.

It is beyond the scope of the current paper to perform the detailed radiative transfer modelling that would be required to discuss this observation in more detail, but qualitatively a steeper slope at longer wavelengths could point to a lower MLR in the past, or, to reverse the timeline, to a recent start of the so-called superwind phase that would indicate the beginning of

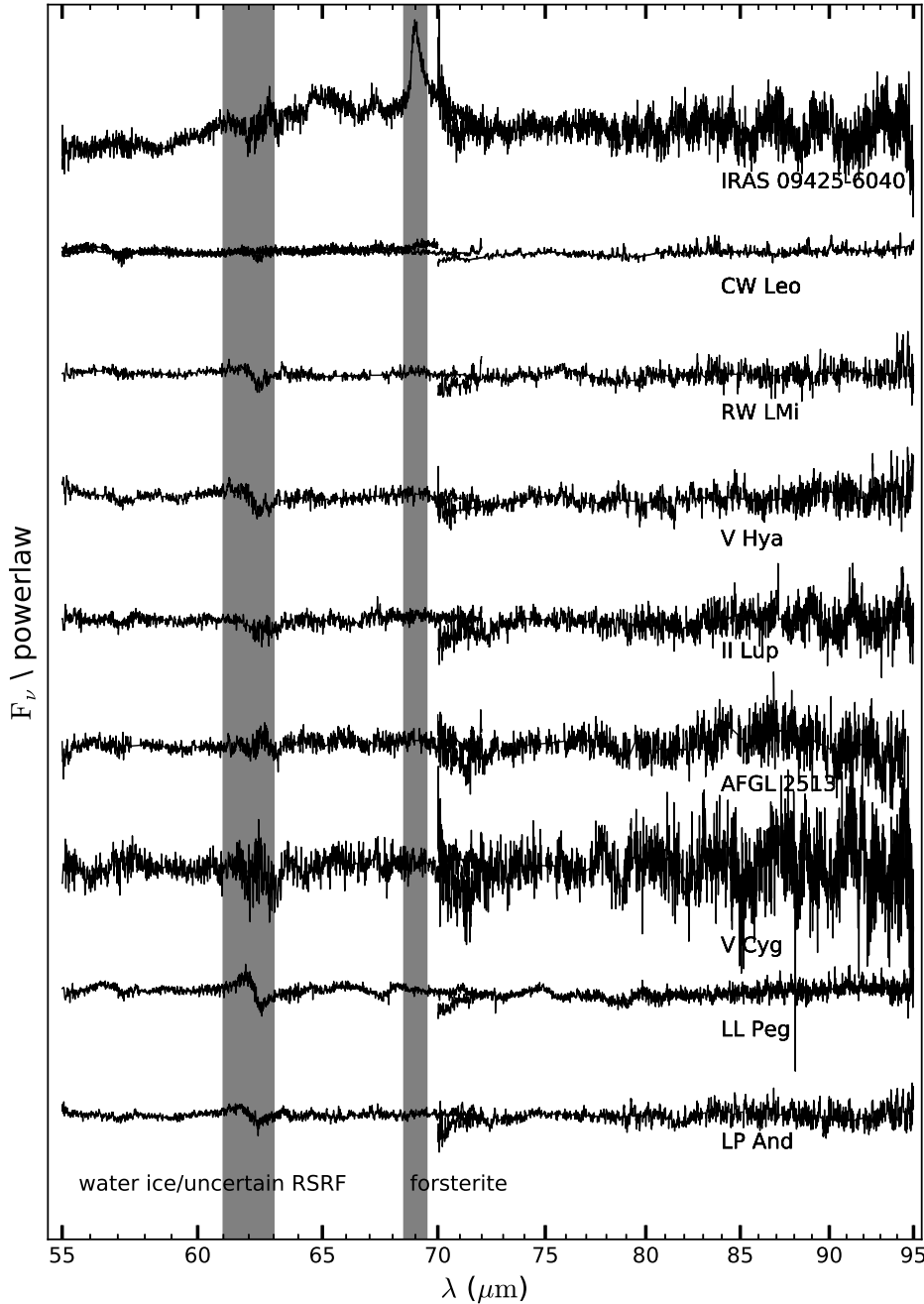


Fig. 8. As Fig. 7 for the C-type targets.

the end of AGB evolution. This scenario was invoked a long time ago (Heske et al. 1990) based on the relative weakness of the lower-J CO lines and has been discussed in the literature since (e.g. Justtanont et al. 1996, 2006, 2013; Decin et al. 2006, 2007; de Vries et al. 2014).

5.2. Solid-state features

The Infrared Space Observatory (ISO) has revolutionised our knowledge of dust spectroscopy (see e.g. the review by Henning 2010). Based on that success one of the aims of the MESS *Herschel* Key Programme (Groenewegen 2007) was to look for (new) dust features. Posch et al. (2005) discuss solid-state features that are potentially observable in the PACS range, and that include some ices and silicate dust species.

Figures 7–9 show the continuum spectra divided by a power law for the M-, C- and S-type targets. This is useful in order to

assess the potential presence of solid-state features. Previously, Sylvester et al. (1999) discussed the spectra of OH/IR stars based on ISO-SWS (2.4–45 μm) and LWS (45–197 μm). In the wavelength region covered by PACS they claim the detection of water ice in emission at 62 μm in OH 127.8, OH 26.5, and AFGL 5379 (all in our sample), and detect forsterite silicate at 69 μm in OH 127.8, OH 26.5, OH 32.8, and AFGL 5379 (all in our sample).

Unfortunately, the 61–63 μm region is a difficult one for PACS as the relative spectral response function (RSRF) is not easy to calibrate due to the presence of a spectral feature in one of the filters in the light path, resulting in a spectral feature that depends on the spatial structure of the source and on the pointing error of the corresponding observation. The variation due to the RSRF can be judged from the spectra of the C-stars where no water ice is expected to be present. The typical shape of the spectra of the M-stars in that region is not

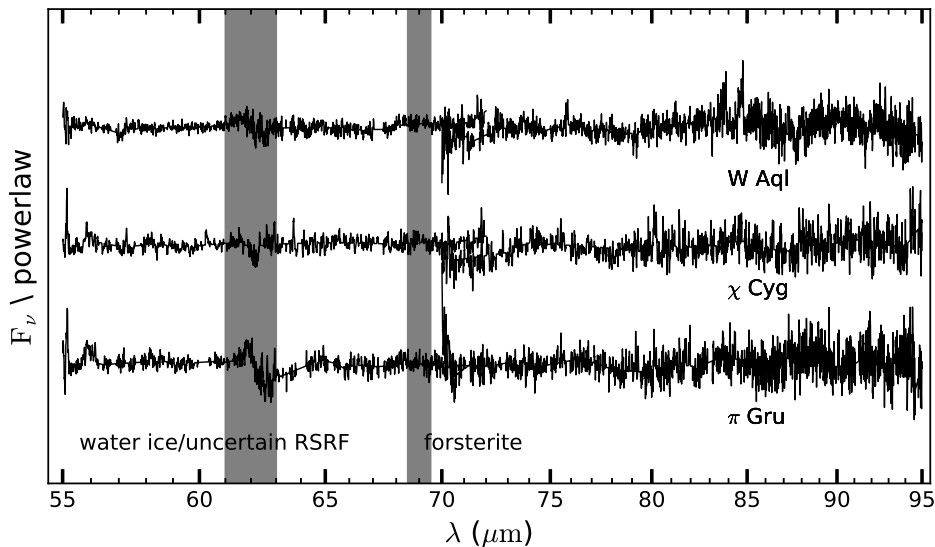


Fig. 9. As Fig. 7 for the S-type targets.

markedly different. Unfortunately, the problematic PACS data in that wavelength region do not allow us to confirm or deny the claim by Sylvester et al. (1999) regarding the presence of water ice in OH 127.8, OH 26.5, and AFGL 5379.

The location and shape of the forsterite feature near $69\ \mu\text{m}$ in PACS spectra of evolved stars has been extensively discussed in Blommaert et al. (2014) and de Vries et al. (2014). No new sources showing forsterite have been found, nor any new possible solid-state features, at least down to a level of $\sim 5\%$ of the continuum.

5.3. Rotational temperatures

A two-component model (or a single temperature when not enough data were available) to trace the excitation temperature is obviously a very crude approximation to the true gas temperature profile in a CSE, which is determined by several heating and cooling mechanisms whose relative contributions vary throughout the CSE (Goldreich & Scoville 1976). It is reassuring to see that for the C-stars where we modelled both CO and HCN the temperatures (the single value, or both hot and cool components) agree within the error bar. The temperatures are relatively uniform between 80 and 120 K for the cool, and between 450 and 650 K for the hot component. This justifies a posteriori a maximum temperature of 500 K in the LTE calculations of Sect. 4.2. The cool component is still relatively warm because the lowest CO transitions ($J = 1-0$ to $3-2$), which trace the outermost parts of the CSE, are outside the SPIRE wavelength range. When no SPIRE spectrum is available, the lowest detectable transition is the $J = 14-13$ transition.

We have compared the rotational temperatures to the gas temperature profiles available in the literature, typically based on detailed studies of individual objects that solved the thermal balance equation in a self-consistent way (Maercker et al. 2016, for R Dor, R Cas, TX Cam, and IK Tau; Danilovich et al. 2014, for W Aql; Schöier et al. 2011, for χ Cyg; Maercker et al. 2008, for W Hya, and IK Tau; Decin et al. 2006, for VY CMa; Schöier & Olofsson 2001, for LP And and R For; Ryde et al. 1999, for II Pup; Groenewegen et al. 1998, for CW Leo; Justtanont et al. 1996, for OH 26.5; and Groenewegen 1994, for OH 32.8). Such a comparison is qualitative only as it assumes that the gas temperature equals the rotational temperature of the CO molecule, which is typically not the case, as there is heating

and cooling by other molecules and the excitation temperature of the different CO transitions are typically not equal. Nevertheless, we find that the hot component traces the gas temperature at 8–10 to 20–30 stellar radii, while the cool component traces the gas temperature in the region 50–150 stellar radii. The two exceptions are OH 26.5 and OH 32.8. For OH 26.5 the hot component is typical for the temperature at ~ 40 stellar radii and the cool temperature of 90 K is actually never reached. Due to the superwind nature of the MLR profile adopted in Justtanont et al. (1996; i.e. a lower MLR in the outer part of the wind which leads to higher temperatures, due to the lower density and smaller photo dissociation radius of water, the major coolant) the temperature never drops below ~ 200 K. This model has been refined by Justtanont et al. (2013) but the corresponding temperature profile has not been published. For OH 32.8 the low temperature of 15 K is only reached at several hundred stellar radii.

6. Summary

PACS and SPIRE spectra are presented for a sample of 40 AGB stars and red supergiants, reduced according to the current state of the art reduction strategies. Molecular lines have been identified and line fluxes measured. The full spectra, and the continuum spectra with all identified lines removed are made available to the community.

In addition, we derive rotational diagrams and rotation temperatures for CO. In future works this will be extended to line radiative transfer modelling for all detected lines (plus literature data). Finally, we measure the slope of the dust continua. In future works this will be extended to dust radiative transfer modelling of the spectra (and other photometric data) over the entire wavelength region.

Acknowledgements. This research has been funded by the Belgian Science Policy Office under contract BR/143/A2/STARLAB. TD acknowledges support from the Fund for Scientific Research (FWO), Flanders, Belgium.

References

- Agúndez, M., Fonfría, J. P., Cernicharo, J., et al. 2012, *A&A*, 543, A48
 Amyay, B., Fayt, A., & Herman, M. 2011, *J. Chem. Phys.*, 135, 234305
 André, P. 2007, *Herschel Space Obs. Prop.*, 49

- Asplund, M., Grevesse, N., Sauval, A. J., & Scott, P. 2009, *ARA&A*, 47, 481
- Barlow, M. 2011, *Herschel Space Obs. Prop.*, 1544
- Blommaert, J. A. D. L., de Vries, B. L., Waters, L. B. F. M., et al. 2014, *A&A*, 565, A109
- Cami, J. 2011, *Herschel Space Obs. Prop.*, 1793
- Cernicharo, J., Waters, L. B. F. M., Decin, L., et al. 2010, *A&A*, 521, L8
- Chen, P., Pearson, J. C., Pickett, H. M., Matsuura, S., & Blake, G. A. 2000, *ApJS*, 128, 371
- Cox, N. 2011, *Herschel Space Obs. Prop.*, 1561
- Cox, N. L. J., Kerschbaum, F., van Marle, A.-J., et al. 2012, *A&A*, 537, A35
- Cristallo, S., Straniero, O., Piersanti, L., & Gobrecht, D. 2015, *ApJS*, 219, 40
- Danilovich, T., Bergman, P., Justtanont, K., et al. 2014, *A&A*, 569, A76
- Danilovich, T., Teyssier, D., Justtanont, K., et al. 2015, *A&A*, 581, A60
- Danilovich, T., De Beck, E., Black, J. H., Olofsson, H., & Justtanont, K. 2016, *A&A*, 588, A119
- Danilovich, T., Lombaert, R., Decin, L., et al. 2017, *A&A*, 602, A14
- De Beck, E., Decin, L., de Koter, A., et al. 2010, *A&A*, 523, A18
- De Beck, E., Lombaert, R., Agúndez, M., et al. 2012, *A&A*, 539, A108
- De Beck, E., Kamiński, T., Patel, N. A., et al. 2013, *A&A*, 558, A132
- Decin, L., Hony, S., de Koter, A., et al. 2006, *A&A*, 456, 549
- Decin, L., Hony, S., de Koter, A., et al. 2007, *A&A*, 475, 233
- Decin, L., Agúndez, M., Barlow, M. J., et al. 2010a, *Nature*, 467, 64
- Decin, L., Justtanont, K., De Beck, E., et al. 2010b, *A&A*, 521, L4
- Decin, L., Royer, P., Cox, N. L. J., et al. 2011, *A&A*, 534, A1
- Decin, L., Cox, N. L. J., Royer, P., et al. 2012, *A&A*, 548, A113
- De Nutte, R., Decin, L., Olofsson, H., et al. 2017, *A&A*, 600, A71
- Desmurs, J.-F., Bujarrabal, V., Lindqvist, M., et al. 2014, *A&A*, 565, A127
- de Vicente, P., Bujarrabal, V., Díaz-Pulido, A., et al. 2016, *A&A*, 589, A74
- de Vries, B. L., Blommaert, J. A. D. L., Waters, L. B. F. M., et al. 2014, *A&A*, 561, A75
- Fonfría, J. P., Cernicharo, J., Richter, M. J., & Lacy, J. H. 2008, *ApJ*, 673, 445
- Gobrecht, D., Cherchneff, I., Sarangi, A., Plane, J. M. C., & Bromley, S. T. 2016, *A&A*, 585, A6
- Goldreich, P., & Scoville, N. 1976, *ApJ*, 205, 144
- Goldsmith, P. F., & Langer, W. D. 1999, *ApJ*, 517, 209
- González Delgado, D., Olofsson, H., Kerschbaum, F., et al. 2003, *A&A*, 411, 123
- Griffin, M. J., Abergel, A., Abreu, A., et al. 2010, *A&A*, 518, L3
- Groenewegen, M. A. T. 1994, *A&A*, 290, 544
- Groenewegen, M. 2007, *Herschel Space Obs. Prop.*, 22
- Groenewegen, M. A. T., & de Jong, T. 1998, *A&A*, 337, 797
- Groenewegen, M. A. T., van der Veen, W. E. C. J., & Matthews, H. E. 1998, *A&A*, 338, 491
- Groenewegen, M. A. T., Sevenster, M., Spoon, H. W. W., & Pérez, I. 2002, *A&A*, 390, 501
- Groenewegen, M. A. T., Waelkens, C., Barlow, M. J., et al. 2011, *A&A*, 526, A162
- Groenewegen, M. A. T., Barlow, M. J., Blommaert, J. A. D. L., et al. 2012, *A&A*, 543, L8
- Habing, H. J., & Olofsson, H., 2003, *Asymptotic Giant Branch Stars* (New-York/Berlin: Springer)
- Henning, T. 2010, *ARA&A*, 48, 21
- Heske, A., Forveille, T., Omont, A., van der Veen, W. E. C. J., & Habing, H. J. 1990, *A&A*, 239, 173
- Hinkle, K. H., Lebzelter, T., & Straniero, O. 2016, *ApJ*, 825, 38
- Höfner, S., & Olofsson, H. 2018, *A&ARv*, 26, 1
- Huggins, P. J., Bachiller, R., Cox, P., & Forveille, T. 1994, *ApJ*, 424, L127
- Justtanont, K. 2011, *Herschel Space Obs. Prop.*, 1968
- Justtanont, K., Skinner, C. J., Tielens, A. G. G. M., Meixner, M., & Baas, F. 1996, *ApJ*, 456, 337
- Justtanont, K., Olofsson, G., Dijkstra, C., & Meyer, A. W. 2006, *A&A*, 450, 1051
- Justtanont, K., Teyssier, D., Barlow, M. J., et al. 2013, *A&A*, 556, A101
- Karakas, A. I., & Lugaro, M. 2016, *ApJ*, 825, 26
- Keene, J., Young, K., Phillips, T. G., Buettingbach, T. H., & Carlstrom, J. E. 1993, *ApJ*, 415, L131
- Kerschbaum, F., Ladjal, D., Ottensamer, R., et al. 2010, *A&A*, 518, L140
- Khouri, T., de Koter, A., Decin, L., et al. 2014a, *A&A*, 561, A5
- Khouri, T., de Koter, A., Decin, L., et al. 2014b, *A&A*, 570, A67
- Kim, H., Wyrowski, F., Menten, K. M., & Decin, L. 2010, *A&A*, 516, A68
- Knapp, G. R., & Morris, M. 1985, *ApJ*, 292, 640
- Knapp, G. R., Crosas, M., Young, K., & Ivezić, Ž. 2000, *ApJ*, 534, 324
- Ladjal, D., Barlow, M. J., Groenewegen, M. A. T., et al. 2010, *A&A*, 518, L141
- Le Bertre, T. 1992, *A&AS*, 94, 377
- Lombaert, R., Decin, L., de Koter, A., et al. 2013, *A&A*, 554, A142
- Lombaert, R., Decin, L., Royer, P., et al. 2016, *A&A*, 588, A124
- Loup, C., Forveille, T., Omont, A., & Paul, J. F. 1993, *A&AS*, 99, 291
- Maercker, M., Schöier, F. L., Olofsson, H., Bergman, P., & Ramstedt, S. 2008, *A&A*, 479, 779
- Maercker, M., Ramstedt, S., Leal-Ferreira, M. L., Olofsson, G., & Floren, H. G. 2014, *A&A*, 570, A101
- Maercker, M., Danilovich, T., Olofsson, H., et al. 2016, *A&A*, 591, A44
- Marigo, P., Ripamonti, E., Nanni, A., Bressan, A., & Girardi, L. 2016, *MNRAS*, 456, 23
- Matsuura, M., Yates, J. A., Barlow, M. J., et al. 2014, *MNRAS*, 437, 532
- Mayer, A., Jorissen, A., Kerschbaum, F., et al. 2013, *A&A*, 549, A69
- Mayer, A., Jorissen, A., Paladini, C., et al. 2014, *A&A*, 570, A113
- Melnick, G. J., Neufeld, D. A., Ford, K. E. S., Hollenbach, D. J., & Ashby, M. L. N. 2001, *Nature*, 412, 160
- Mečina, M., Kerschbaum, F., Groenewegen, M. A. T., et al. 2014, *A&A*, 566, A69
- Molinari, S. 2007, *Herschel Space Obs. Prop.*, 82
- Molinari, S. 2010, *Herschel Space Obs. Prop.*, 1172
- Molinari, S., Swinyard, B., Bally, J., et al. 2010, *PASP*, 122, 314
- Molinari, S., Schisano, E., Elia, D., et al. 2016, *A&A*, 591, A149
- Molster, F. J., Yamamura, I., Waters, L. B. F., et al. 2001, *A&A*, 366, 923
- Müller, H. S. P., Thorwirth, S., Roth, D. A., & Winniewisser, G. 2001, *A&A*, 370, L49
- Olivier, E. A., Whitelock, P., & Marang, F. 2001, *MNRAS*, 326, 490
- Olofsson, H., González Delgado, D., Kerschbaum, F., & Schöier, F. L. 2002, *A&A*, 391, 1053
- Olofsson, H., Bergman, P., & Lindqvist, M. 2015, *A&A*, 582, A102
- Ott, S. 2010, in *Astronomical Data Analysis Software and Systems XIX*, eds. Y. Mizumoto, K.-I. Morita, & M. Ohishi, *ASP Conf. Ser.*, 434, 139
- Pickett, H. M., Poynter, R. L., Cohen, E. A., et al. 1998, *J. Quant. Spectr. Rad. Transf.*, 60, 883
- Pilbratt, G. L., Riedinger, J. R., Passvogel, T., et al. 2010, *A&A*, 518, L1
- Pogltisch, A., Waelkens, C., Geis, N., et al. 2010, *A&A*, 518, L2
- Posch, T., Kerschbaum, F., Richter, H., & Mutschke, H. 2005, *ESA SP*, ed. A. Wilson, 577, 257
- Ramos-Medina, J., Sánchez Contreras, C., García-Lario, P., et al. 2018, *A&A*, 611, A41
- Ramstedt, S., & Olofsson, H. 2014, *A&A*, 566, A145
- Ramstedt, S., Schöier, F. L., & Olofsson, H. 2009, *A&A*, 499, 515
- Reid, M. J., Menten, K. M., Brunthaler, A., et al. 2014, *ApJ*, 783, 130
- Richards, A. M. S., Etoke, S., Gray, M. D., et al. 2012, *A&A*, 546, A16
- Royer, P. 2011, *Herschel Space Obs. Prop.*, 1556
- Royer, P., Decin, L., Wesson, R., et al. 2010, *A&A*, 518, L145
- Ryde, N., Schöier, F. L., & Olofsson, H. 1999, *A&A*, 345, 841
- Saberi, M., Vlemmings, W. H. T., De Beck, E., Montez, R., & Ramstedt, S. 2018, *A&A*, 612, L11
- Sahai, R., & Chronopoulos, C. K. 2010, *ApJ*, 711, L53
- Sahai, R., Sugerman, B. E. K., & Hinkle, K. 2009, *ApJ*, 699, 1015
- Schöier, F. L., & Olofsson, H. 2001, *A&A*, 368, 969
- Schöier, F. L., Olofsson, H., & Lundgren, A. A. 2006, *A&A*, 454, 247
- Schöier, F. L., Bast, J., Olofsson, H., & Lindqvist, M. 2007, *A&A*, 473, 871
- Schöier, F. L., Maercker, M., Justtanont, K., et al. 2011, *A&A*, 530, A83
- Schöier, F. L., Ramstedt, S., Olofsson, H., et al. 2013, *A&A*, 550, A78
- Smith, N., Hinkle, K. H., & Ryde, N. 2009, *AJ*, 137, 3558
- Sylvester, R. J., Kemper, F., Barlow, M. J., et al. 1999, *A&A*, 352, 587
- van der Veen, W. E. C. J., Huggins, P. J., & Matthews, H. E. 1998, *ApJ*, 505, 749
- Van de Sande, M., Decin, L., Lombaert, R., et al. 2018, *A&A*, 609, A63
- van Langevelde, H. J., van der Heiden, R., & van Schooneveld, C. 1990, *A&A*, 239, 193
- van Leeuwen, F. 2007, *A&A*, 474, 653
- Velilla Prieto, L., Sánchez Contreras, C., Cernicharo, J., et al. 2017, *A&A*, 597, A25
- Wong, K. T., Menten, K. M., Kamiński, T., & Wyrowski, F. 2015, in *Why Galaxies Care about AGB Stars III: A Closer Look in Space and Time*, eds. F. Kerschbaum, R. F. Wing, & J. Hron, *ASP Conf. Ser.*, 497, 141
- Woods, P. M., Schöier, F. L., Nyman, L.-Å., & Olofsson, H. 2003, *A&A*, 402, 617
- Zhang, Y., Kwok, S., & Dinh-V-Trung, S. 2009, *ApJ*, 691, 1660
- Ziurys, L. M., Tenenbaum, E. D., Pulliam, R. L., Woolf, N. J., & Milam, S. N. 2009, *ApJ*, 695, 1604

Appendix A: Observations

Table A.1 presents the basic information of all gdata sets used in the present paper. Listed are the target name (also see Table 2),

name of the PI (see Sect. 2.1 for a description of the programs), *Herschel's* unique Observation Identification number, and a description of the data set.

Table A.1. Specifications of observations sample targets.

Identifier	PI	Obs. ID	Observation	Remark
<i>AGB-stars</i>				
WX Psc	Groenewegen	1342202122	PACS B2A, short R1	
	Groenewegen	1342202121	PACS B2B, long R1	Mismatch with 70 μ m bolometer flux
	Barlow	1342246973	SPIRE FTS	Small mismatch with PACS spectrum
R Scl	Groenewegen	1342188486/1342188487	PACS image 70, 160	
	Groenewegen	1342189545	SPIRE FTS	Mismatch with 500 μ m bolometer flux
	Groenewegen	1342213264/1342213265	PACS image 70, 160	
OH 127.8 +0.0	Groenewegen	1342188657	SPIRE image	
	Lombaert	1342189956 - 1342189961	PACS full spectrum	
	Justtanont	1342268319	SPIRE FTS	Alternative background subtraction
o Cet	Groenewegen	1342189181/1342189182	PACS image 70, 160	
	Molinari	1342226650/1342226651	SPIRE image	
	Groenewegen	1342213287	PACS B2A, short R1	
IK Tau	Groenewegen	1342213286	PACS B2B, long R1	
	Groenewegen	1342189546	SPIRE FTS	
	Groenewegen	1342190335/1342190336	PACS image 70, 160	
R Dor	Groenewegen	1342189423	SPIRE image	
	Groenewegen	1342203680	PACS B2A, short R1	
	Groenewegen	1342203681	PACS B3A	
TX Cam	Groenewegen	1342203679	PACS B2B, long R1	
	Groenewegen	1342192176	SPIRE FTS	Mismatch with 250 μ m bolometer flux small mismatch with PACS spectrum
	Groenewegen	1342190343/1342190344	PACS image 70, 160	
IRAS 09425–6040	Groenewegen	1342248696/1342248697	PACS image 100, 160	
	Groenewegen	1342191180	SPIRE image	
	Groenewegen	1342197794	PACS B2A, short R1	
CW Leo	Groenewegen	1342197795	PACS B2B, long R1	
	Barlow	1342245114	SPIRE FTS	
	Groenewegen	1342197685/1342197686	PACS image 70, 160	
RW LMi	Groenewegen	1342188164	SPIRE image	
	Groenewegen	1342225856	PACS B2A, short R1	summed 3 \times 3 spaxel
	Groenewegen	1342225855	PACS B2B, long R1	summed 3 \times 3 spaxel
V Hya	Groenewegen	1342251300	SPIRE FTS	Alternative background subtraction offset with PACS spectrum
	Groenewegen	1342217395/1342217396	PACS image 70, 160	
	Royer	1342242742/1342242743	PACS image 100	
W Hya	Groenewegen	1342225564	PACS B2A, short R1	
	Groenewegen	1342225563	PACS B2B, long R1	
	Groenewegen	1342186964	PACS B2A, B3A, full R1	Extended source
W Hya	Groenewegen	1342186965	PACS B2B	Extended source
	Groenewegen	1342197466	SPIRE FTS	Extended source
	Groenewegen	1342186298/1342186299	PACS image 70, 160	
W Hya	Groenewegen	1342197709/1342197710	PACS image 100	
	Groenewegen	1342207040	SPIRE image	
	Groenewegen	1342197800	PACS B2A, short R1	
W Hya	Groenewegen	1342197799	PACS B2B, long R1	
	Groenewegen	1342198264	SPIRE FTS	
	Groenewegen	1342210620/1342210621	PACS image 70, 160	
W Hya	Groenewegen	1342206689	SPIRE image	
	Groenewegen	1342197791	PACS B2A, short R1	
	Groenewegen	1342197790	PACS B2B, long R1	
W Hya	Barlow	1342247570	SPIRE FTS	
	Groenewegen	1342211997/1342211998	PACS image 70, 160	
	Groenewegen	1342188160	SPIRE image	
W Hya	Groenewegen	1342212604	PACS B2A, short R1	
	Groenewegen	1342203453	PACS B2B	

Table A.1. continued.

Identifier	PI	Obs. ID	Observation	Remark
II Lup	Groenewegen	1342223808	PACS long R1	
	Groenewegen	1342189116	SPIRE FTS	
	Groenewegen	1342213848/1342213849	PACS image 70, 160	
	Groenewegen	1342189519	SPIRE image	
	Groenewegen	1342215686	PACS B2A, short R1	
	Groenewegen	1342215685	PACS B2B, long R1	Mismatch with 70, 160 μm bolometer flux
	Barlow	1342251281	SPIRE FTS	Alternative background subtraction
X Her	Groenewegen	1342190247/1342190248	PACS image 70, 160	
	Groenewegen	1342197802	PACS B2A, short R1	
	Groenewegen	1342202120	PACS B2B, long R1	
AFGL 5379	Groenewegen	1342188322/1342188323	PACS image 70, 160	
	Groenewegen	1342228537	PACS B2A, short R1	Mispointing, one spaxel
	Groenewegen	1342228538	PACS B2B, long R1	Mispointing, one spaxel
	Justtanont	1342268287	SPIRE FTS	Alternative background subtraction offset with PACS spectrum
OH 21.5 +0.5	Molinari	1342204368/1342204369	PACS image 70, 160	
	Justtanont	1342268778	PACS B2A, short R1	Mispointing, one spaxel
	Justtanont	1342268748	PACS B2B, long R1	Mispointing, one spaxel mismatch with 70, 160 μm bolometer flux offset with PACS spectrum
OH 26.5 +0.6	Justtanont	1342268311	SPIRE FTS	Alternative background subtraction
	Molinari	1342218642/1342218643	PACS image 70, 160	
	Molinari	1342218642/1342218643	SPIRE image	
	Groenewegen	1342207777	PACS B2A, short R1	
	Groenewegen	1342207776	PACS B2B, long R1	
	Barlow	1342243624	SPIRE FTS	Alternative background subtraction Mismatch with 350, 500 μm bolometer flux
OH 30.1 -0.7	Groenewegen	1342191817/1342191818	PACS image 70, 160	
	Groenewegen	1342218696/1342218697	SPIRE image	
	Justtanont	1342269305	PACS B2A, short R1	c1 spaxel, inhomogeneous background
	Justtanont	1342269304	PACS B2B, long R1	c1 spaxel, inhomogeneous background
	Justtanont	1342268316	SPIRE FTS	Alternative background subtraction
IRAS 18488-0107	Molinari	1342186275/1342186276	PACS image 70, 160	
	Molinari	1342186275/1342186276	SPIRE image	
	Justtanont	1342268791	PACS B2A, short R1	
	Justtanont	1342268792	PACS B2B, long R1	Mismatch with 70, 160 μm bolometer flux
OH 32.8 -0.3	Justtanont	1342268317	SPIRE FTS	Alternative background subtraction
	Molinari	1342218692/1342218693	PACS image 70, 160	
	Molinari	1342218692/1342218693	SPIRE image	
	Justtanont	1342268793	PACS B2A, short R1	
	Justtanont	1342268794	PACS B2B, long R1	Mismatch with 70, 160 μm bolometer flux
	Justtanont	1342268318	SPIRE FTS	Alternative background subtraction
R Aql	Molinari	1342218692/1342218693	PACS image 70, 160	
	Molinari	1342218692/1342218693	SPIRE image	
	Cami	1342243900	PACS B2A, short R1	
	Molinari	1342207030/1342207031	PACS image 70, 160	
IRAS 19067+0811	Molinari	1342207030/1342207031	SPIRE image	
	Justtanont	1342268797	PACS B2A, short R1	
	Justtanont	1342268798	PACS B2B, long R1	
	Justtanont	1342268308	SPIRE FTS	Alternative background subtraction offset with PACS spectrum
W Aql	Molinari	1342207030/1342207031	PACS image 70, 160	
	Molinari	1342207030/1342207031	SPIRE image	
	Groenewegen	1342209731	PACS B2A, short R1	
GY Aql	Groenewegen	1342209732	PACS B2B, long R1	
	Groenewegen	1342194084/1342194085	PACS image 70, 160	
	OBSherschell	1342268638	PACS B2A, short R1	
χ Cyg	OBSherschell	1342268449	PACS B2B, long R1	
	Groenewegen	1342198177	PACS B2A, short R1	
	Groenewegen	1342198176	PACS B2B, long R1	
	Groenewegen	1342188320/1342188321	PACS image 70, 160	

Table A.1. continued.

Identifier	PI	Obs. ID	Observation	Remark
RR Aql	OBSherschell	1342269414	PACS B2A, short R1	
V1943 Sgr	OBSherschell	1342268730	PACS B2A, short R1	
	OBSherschell	1342268569	PACS B2B, long R1	
	OBSherschell	1342268314	SPIRE FTS	
	Groenewegen	1342208468/1342208469	PACS image 70, 160	
AFGL 2513	OBSherschell	1342270010	PACS B2A, short R1	
	OBSherschell	1342269936	PACS B2B, long R1	
IRC -10 529	OBSherschell	1342269916	PACS B2A, short R1	
	OBSherschell	1342269510	PACS B2B, long R1	Mismatch with 70 μ m bolometer flux
	OBSherschell	1342216902	SPIRE FTS	
	Groenewegen	1342196034/1342196035	PACS image 70, 160	
T Mic	OBSherschell	1342268729	PACS B2A, short R1	
	OBSherschell	1342268788	PACS B2B, long R1	
	Groenewegen	1342193036/1342193037	PACS image 70, 160	
V Cyg	Groenewegen	1342208939	PACS B2A, short R1	
	Groenewegen	1342208940	PACS B2B, long R1	
	Groenewegen	1342188462/1342188463	PACS image 70, 160	
T Cep	Cami	1342246557	PACS B2A, short R1	
	André	1342188652/1342188653	PACS image 70, 160	
	André	1342188652/1342188653	PACS image 70, 160	
EP Aqr	OBSherschell	1342270639	PACS B2A, short R1	
	OBSherschell	1342270684	PACS B2B, long R1	
	Groenewegen	1342195460/1342195461	PACS image 70, 160	
	Cox	1342257155/1342257156	PACS image 100, 160	
π Gru	Groenewegen	1342210397	PACS B2A, short R1	
	Groenewegen	1342210398	PACS B2B, long R1	
	Groenewegen	1342196799/1342196800	PACS image 70, 160	
	Groenewegen	1342193791	SPIRE image	
LL Peg	Groenewegen	1342199417	PACS B2A, short R1	
	Groenewegen	1342199418	PACS B2B, long R1	
	Groenewegen	1342189126	SPIRE FTS	Small mismatch with PACS spectrum
	Groenewegen	1342188378/1342188379	PACS image 70, 160	
	Royer	1342237362/1342237363	PACS image 100, 160	
	Groenewegen	1342188178	SPIRE image	
LP And	Groenewegen	1342212512	PACS B2A, short R1	
	Groenewegen	1342212513	PACS B2B, long R1	
	Barlow	1342246288	SPIRE FTS	
	Groenewegen	1342188490/1342188491	PACS image 70, 160	
R Cas	Groenewegen	1342212576	PACS B2A, short R1	
	Groenewegen	1342212577	PACS B2B, long R1	
	Barlow	1342246981	SPIRE FTS	
	Groenewegen	1342222422/1342222423	PACS image 70, 160	
	Royer	1342237158/1342237159	PACS image 100, 160	
	Groenewegen	1342188578	SPIRE image	
<i>Red Super Giants</i>				
α Ori	Groenewegen	1342218757	PACS B2A, short R1	
	Groenewegen	1342218756	PACS B2B, long R1	
	Groenewegen	1342193663	SPIRE FTS	Mismatch with 250 μ m bolometer flux Mismatch with PACS spectrum
	Groenewegen	1342204435/1342204436	PACS image 70, 160	
	Royer	1342242656/1342242657	PACS image 100, 160	
	Groenewegen	1342192099	SPIRE image	
VY CMa	Groenewegen	1342186653	PACS B2A, B3A, full R1	
	Groenewegen	1342186654	PACS B2B	
	Groenewegen	1342192834	SPIRE FTS	
	Groenewegen	1342194070/1342194071	PACS image 70, 160	
NML Cyg	Groenewegen	1342198175	PACS B2A, short R1	
	Groenewegen	1342198174	PACS B2B, long R1	
	Barlow	1342243592	SPIRE FTS	
	Groenewegen	1342195485/1342195486	PACS image 70, 160	

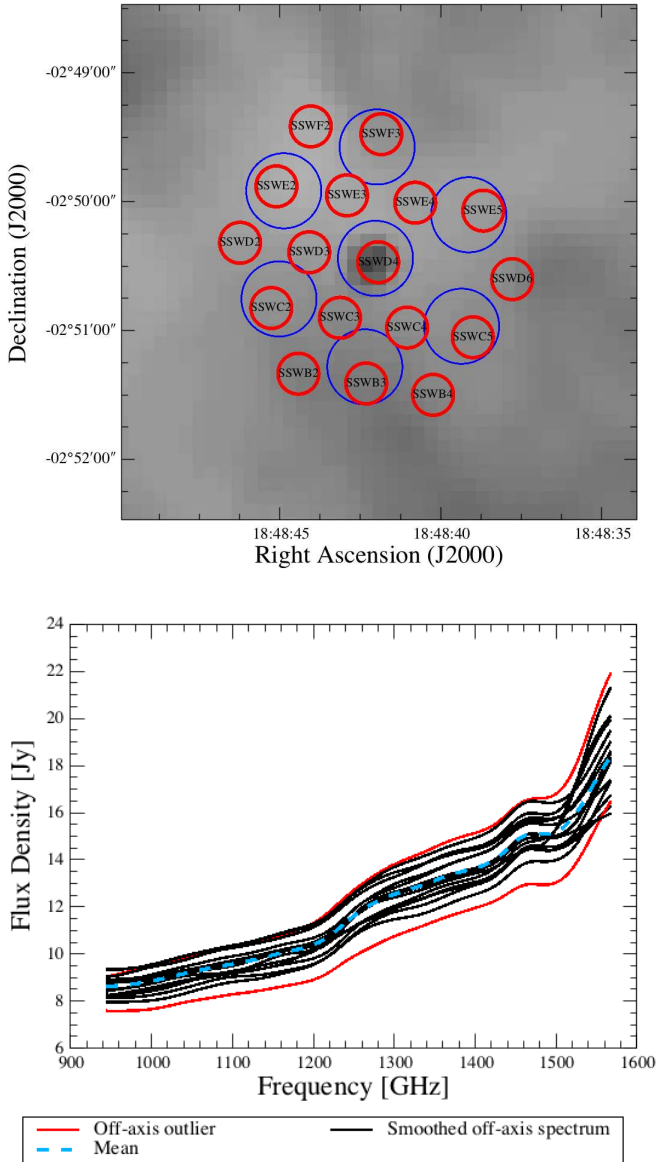


Fig. B.1. *Top panel:* footprint of the SPIRE spectrometer detectors on the sky for OH 30.1–0.7. The blue and red circles represent the beams of the SLW and SSW arrays, respectively (the SSW arrays are identified individually). Two SSW detectors are not considered for background subtraction, and are not represented, which explains the apparent asymmetry of the SSW detector array. *Lower panel:* smoothed off-axis detector intensities and mean off-axis intensities for the SSW array. The black and red curves represent the smoothed spectra measured in the off-axis detectors, i.e. off-source. The spectra marked in red at the edge of the distribution are not used for background subtraction. The others (in black) are averaged, and the average (dotted blue curve) is used for background subtraction.

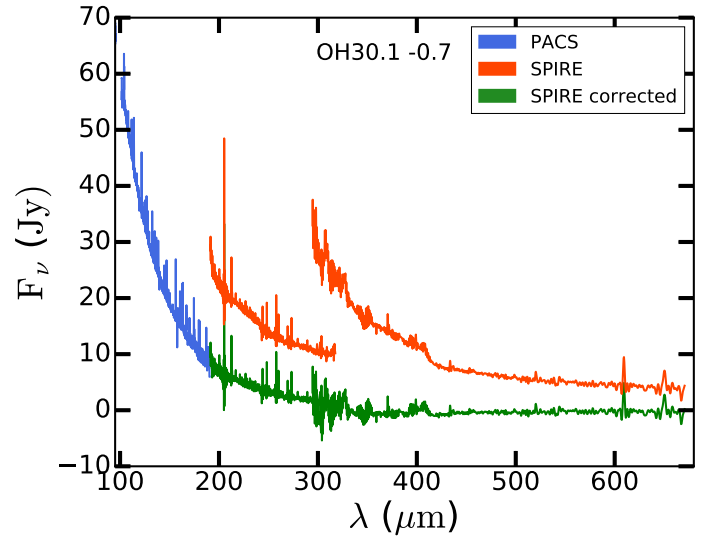


Fig. B.2. Effect of the background correction on the SPIRE spectrum of OH 30.1–0.7.

Appendix B: SPIRE background subtraction

The correction of the spectral shape of the SPIRE spectra that suffer from high background contamination was done by the HIPE *SpectrometerBackgroundSubtraction* script. This method is illustrated below for OH 30.1–0.7.

The top panel in Fig. B.1 shows the footprint of the SPIRE spectrometer on the SPIRE image of OH 30.1–0.7 at 250 μm . The off-axis detectors that surround the on-source central detector were used to measure the sky background. This is done by smoothing the off-axis detectors with a wide kernel to extract low-frequency background information from the data. The smoothed spectra of the different detectors were visually inspected and the most outlying shapes were rejected, as illustrated in the lower panel in Fig. B.1. The off-axis detectors that were used for OH 30.1–0.7 and the other targets are listed in Table B.1. The large-scale shape that arises from the averaging of the remaining off-axis spectra is then subsequently subtracted from the on-source spectrum. Figure B.2 shows that the corrected spectrum closely matches the long wavelength end of the PACS spectrum and that the discontinuity between the SSW and SLW bands has disappeared.

Subtracting the bright off-axis spectrum from a bright background emission may introduce an extra source of uncertainty to the absolute and relative flux calibration of the SPIRE spectra and the analysis of both the corrected continuum and the SPIRE spectral lines must be performed with care.

Table B.1. SPIRE bolometers used for the background subtraction of the spectra of the background contaminated sources.

Name	SSW	SLW
OH 127.8 +0.0	B2, B3, B4	B2, B3
	C2, C5	C2, C4
	D2, D6	D2, D3
	E2, E5	
	F2, F3	
TX Cam	B2, B3, B4	B2, B3
	C2, C5	C2, C4
	D2, D6	D2, D3
	E2, E5	
	F2, F3	
II Lup	B2, B3, B4	B2, B3
	C2, C5	C2, C4
	D2, D6	D3
	E2, E5	
	F2, F3	
AFGL 5379	B2, B3, B4	B2, B3
	C2, C5	C2, C4
	D2, D6	D2, D3
	E2, E5	
	F2, F3	
OH21.5 +0.5	B2, B3, B4	B2, B3
	C2, C5	C2, C4
	D2, D6	D2
	E2, E5	
	F2, F3	
OH26.6 +0.6	B2, B3, B4	B2, B3
	C2, C5	C2, C4
	D2, D6	D2, D3
	E2, E5	
	F2, F3	
OH30.1 -0.7	B2, B3, B4	B2, B3
	C2, C5	C2
	D2, D6	D3
	E2, E5	
	F5	
IRAS 18488-0107	B2, B3, B4	B2, B3
	C2, C5	C2, C4
	D2, D6	D2, D3
	E2	
	F2	
OH32.8 -0.3	B3, B4	B2, B3
	C5	C2
	D2, D6	D2
	E2, E5	
	F2, F3	
IRAS 19067+0811	B2, B3, B4	B2, B3
	C2, C5	C2, C4
	D2, D6	D2, D3
	E2, E5	
	F2, F3	

Appendix C: Population-temperature diagrams

This appendix shows the rotation diagrams for all sources, following the methodology outlined in Sect. 4.3. Rotational

temperatures are listed in Table 6. Red and yellow points are excluded from the fitting (see Sect. 4.3).

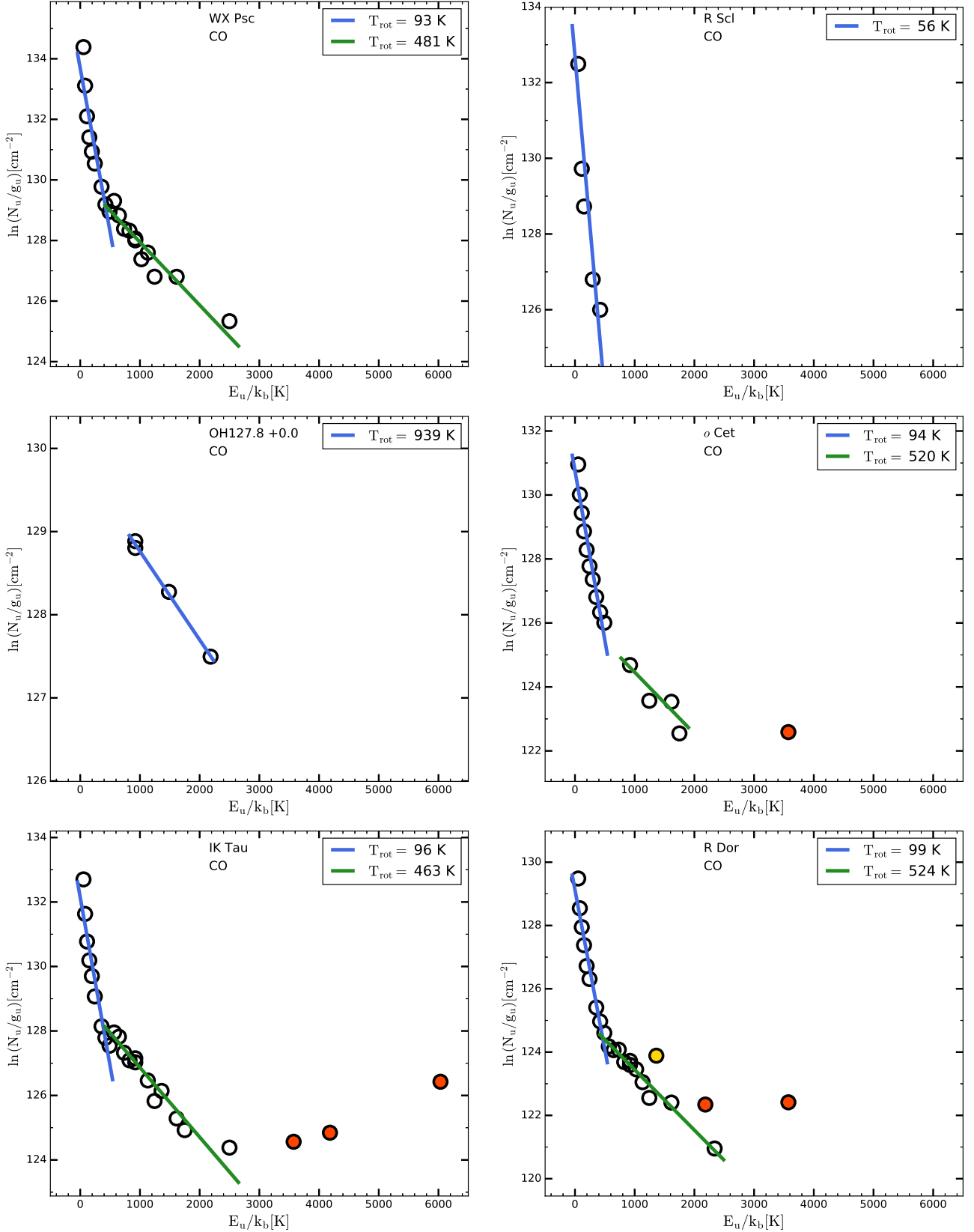


Fig. C.1. CO population-temperature diagrams. Yellow and red points are excluded from the fit, see Sect. 4.3.

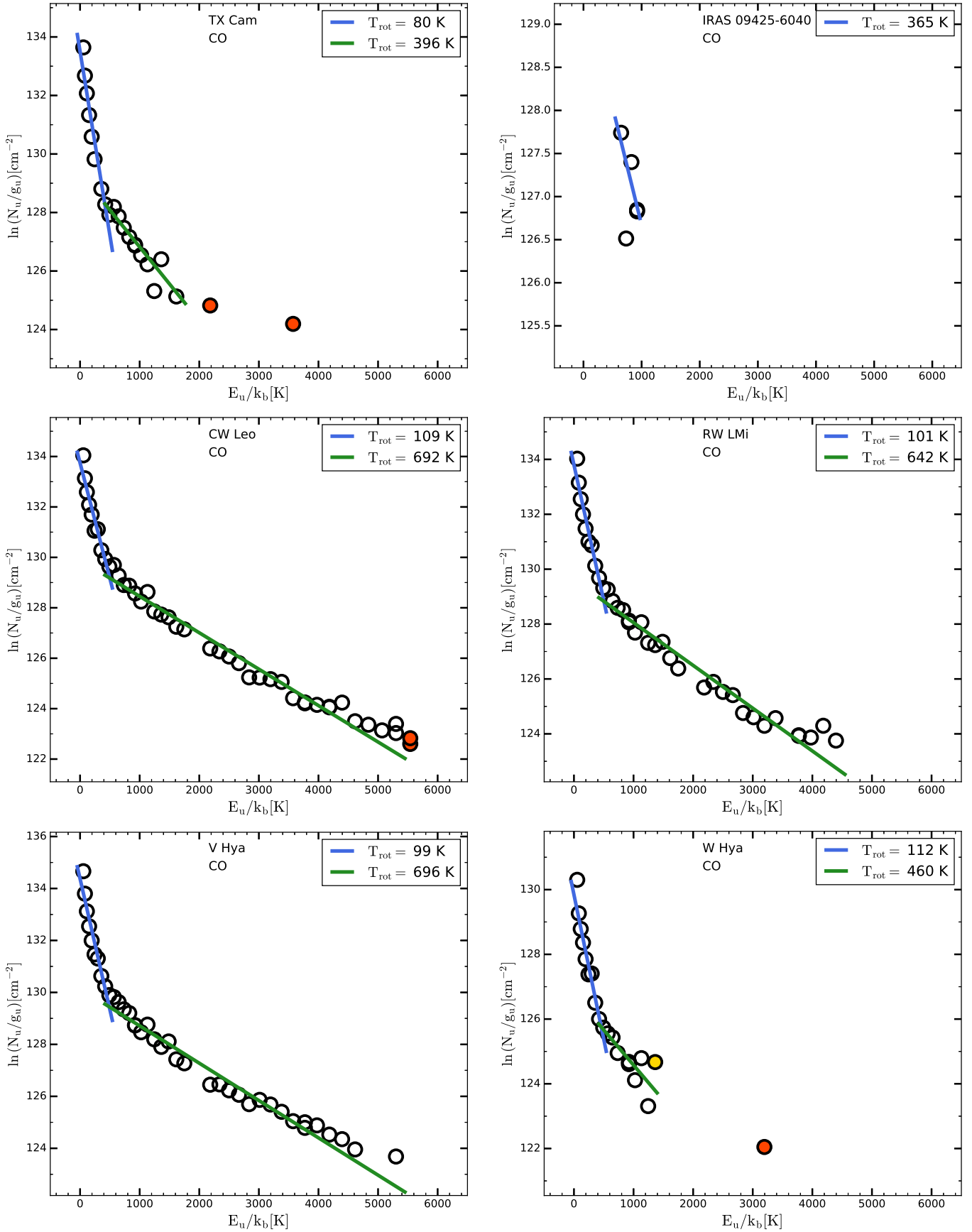


Fig. C.1. continued.

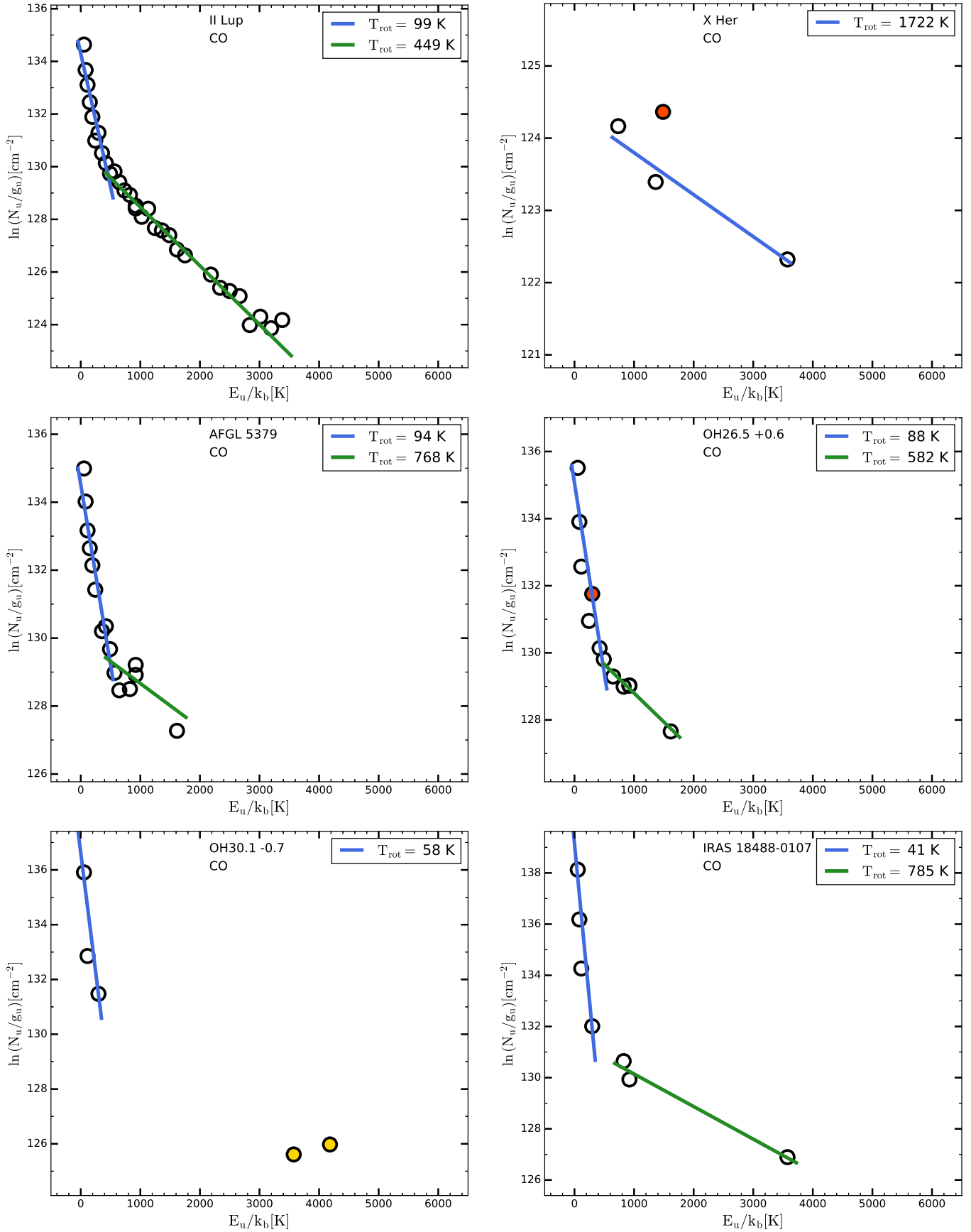


Fig. C.1. continued.

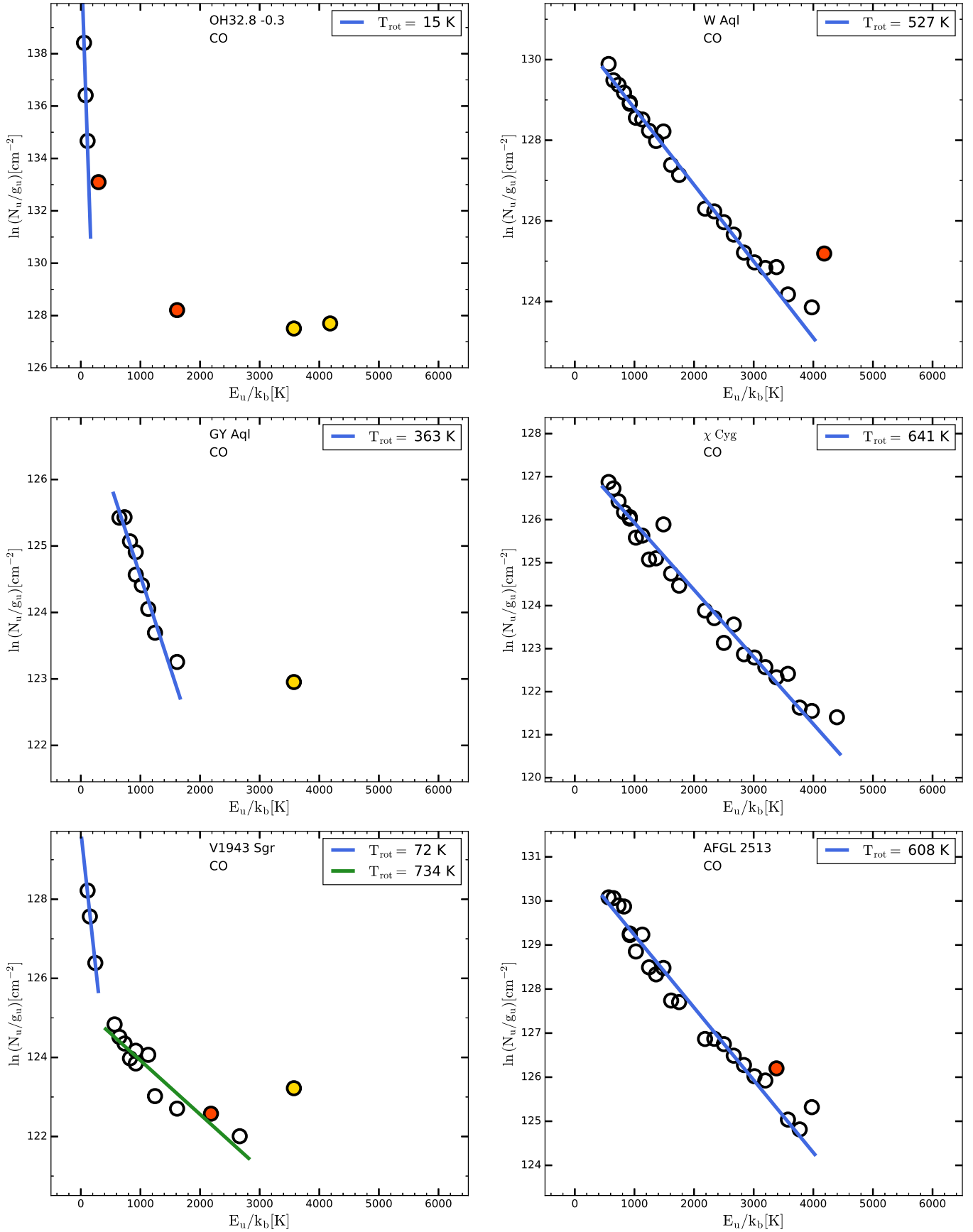


Fig. C.1. continued.

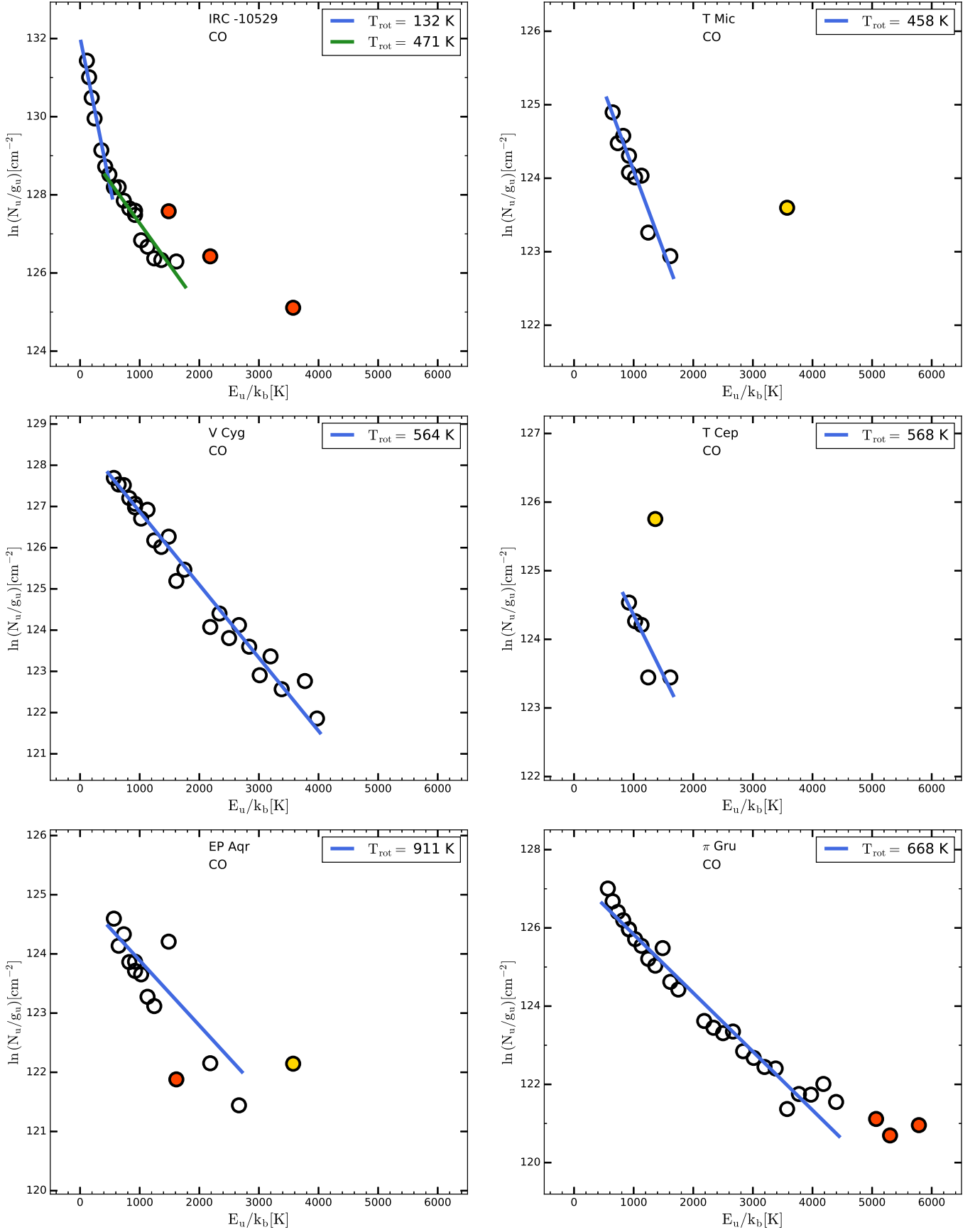


Fig. C.1. continued.

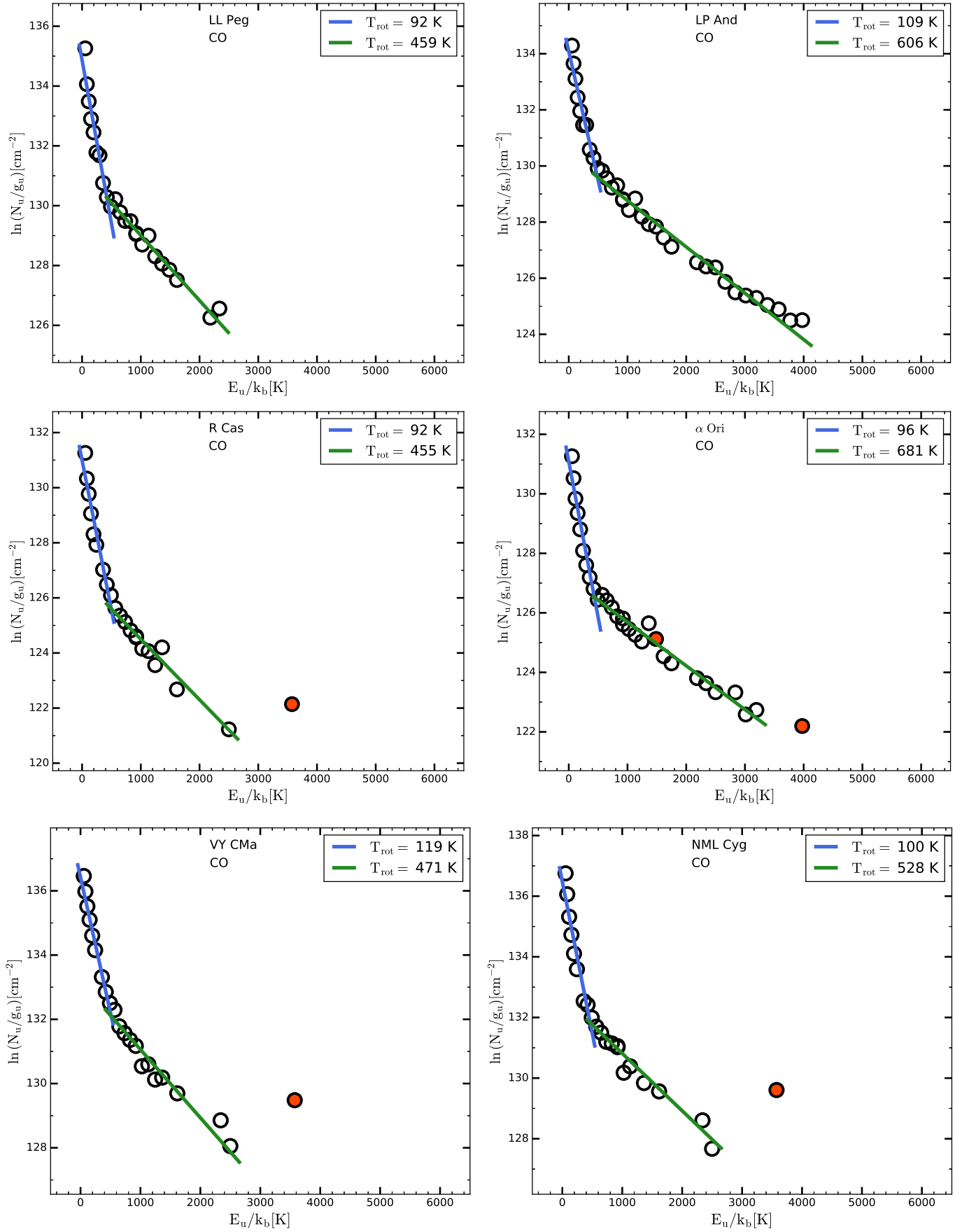


Fig. C.1. continued.

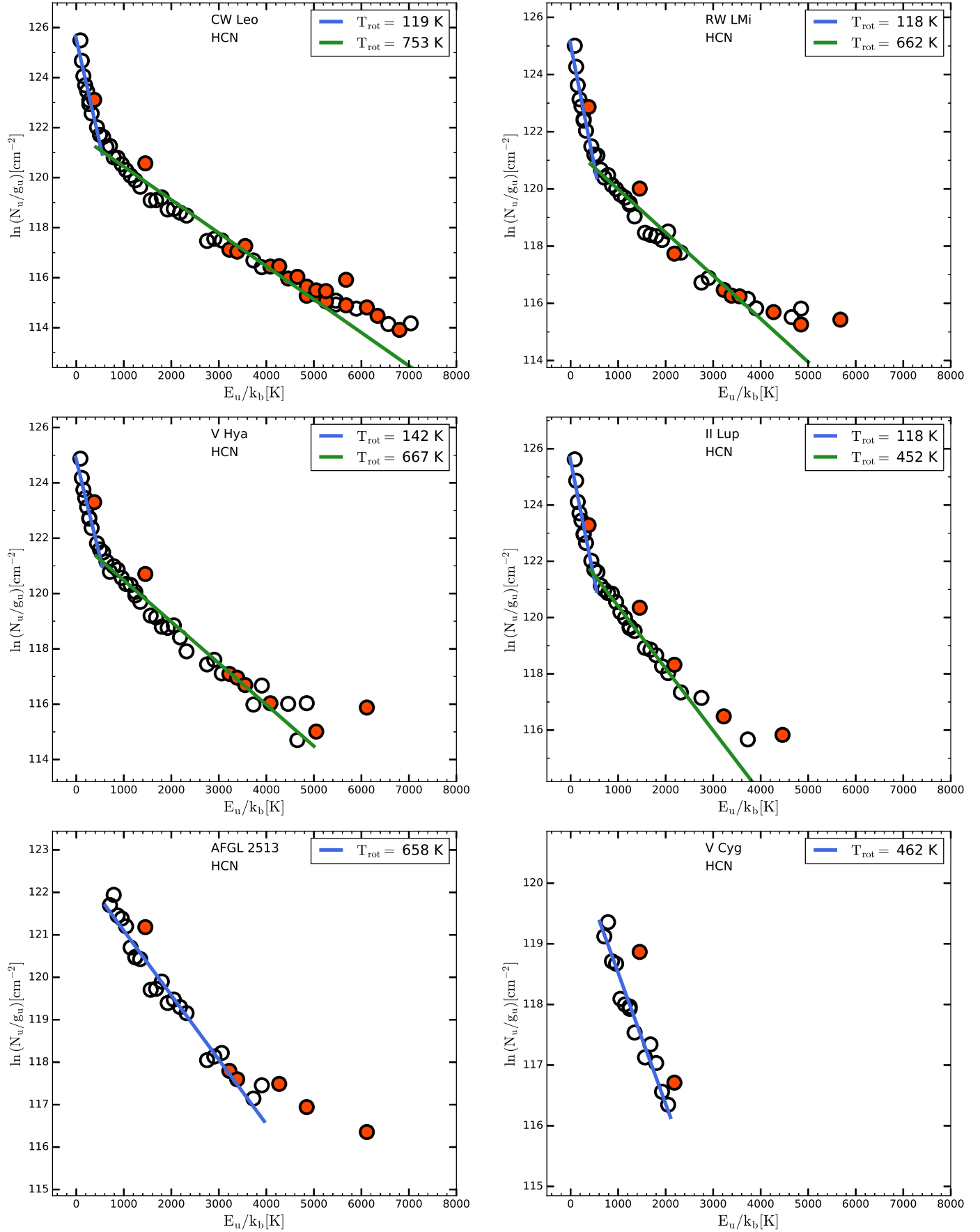


Fig. C.2. HCN population-temperature diagrams for C-type stars.

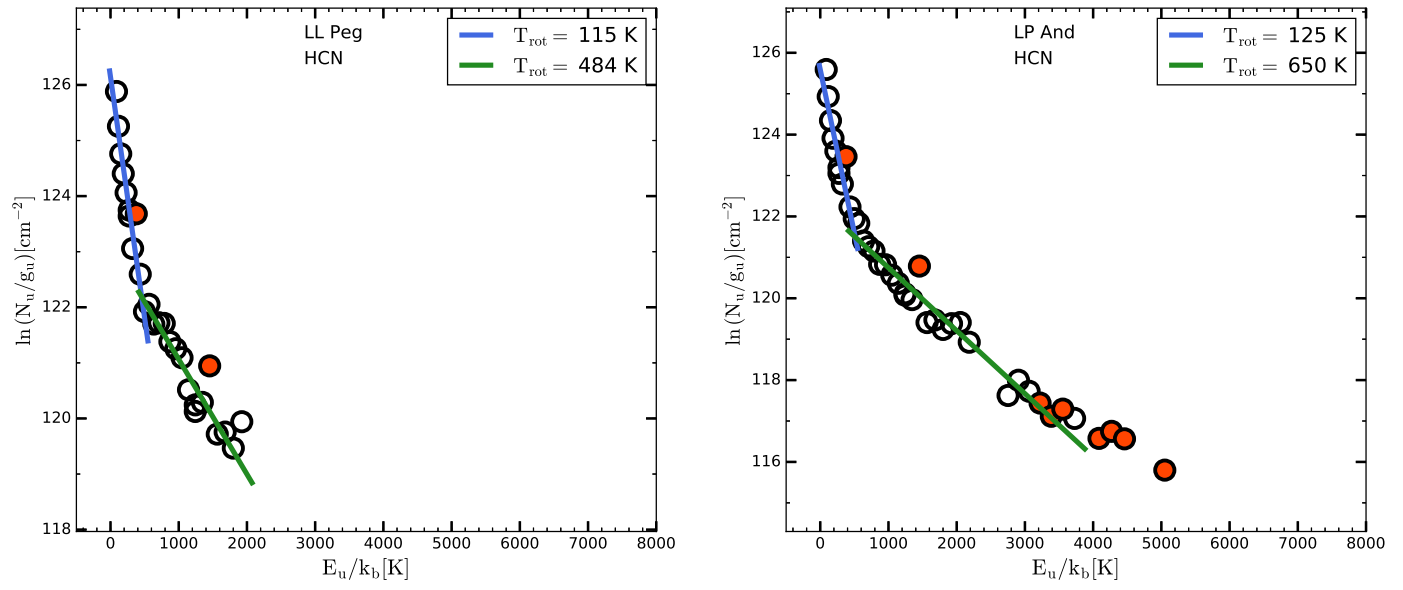


Fig. C.2. continued.

Appendix D: Power law fitting

This appendix shows the continuum spectra fitted with a segmented power law, following the methodology outlined in Sect. 4.5. The indices of the power law are listed in Table 7.

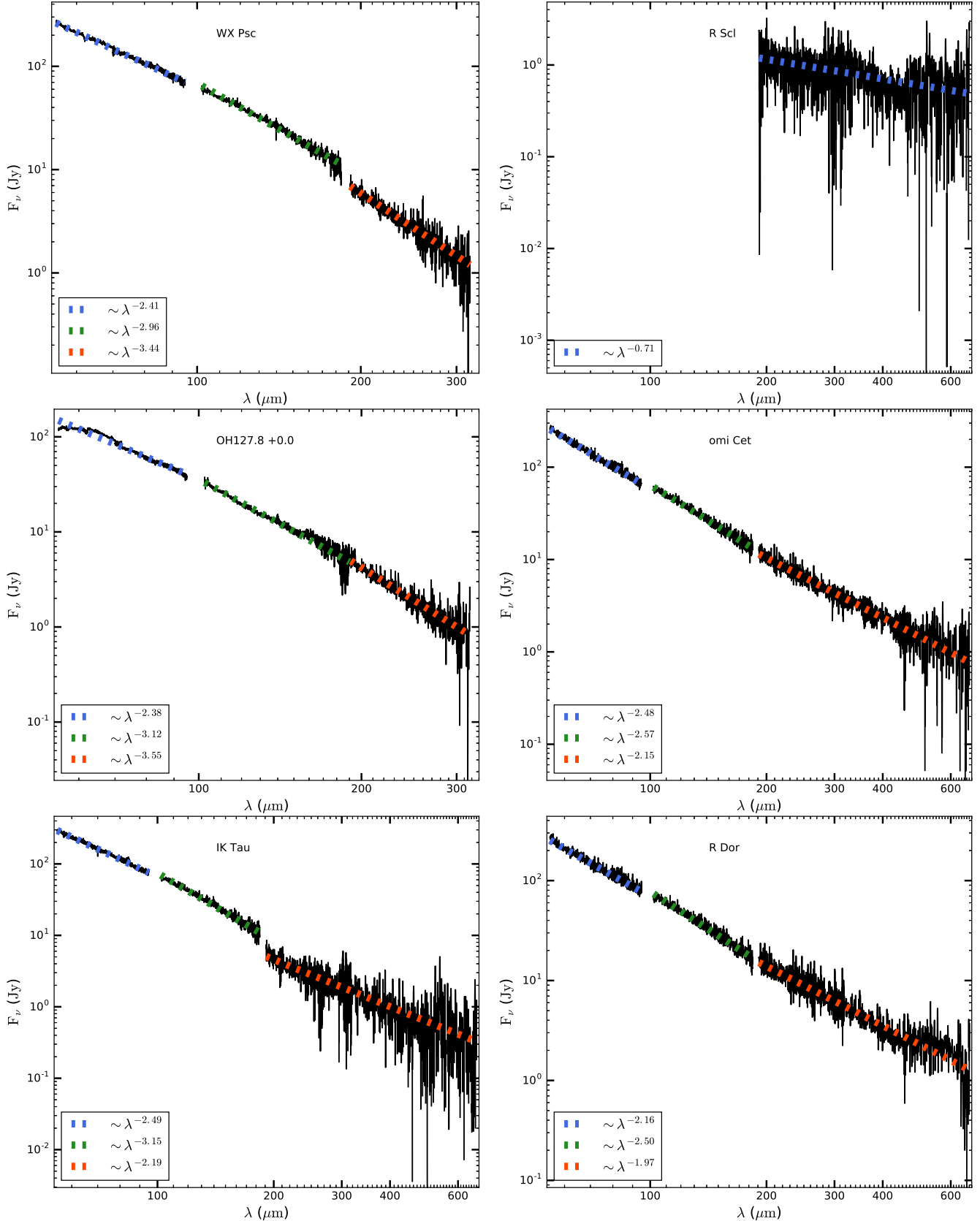


Fig. D.1. Power law fits to three segments of a full PACS and SPIRE line-clipped continuum spectrum.

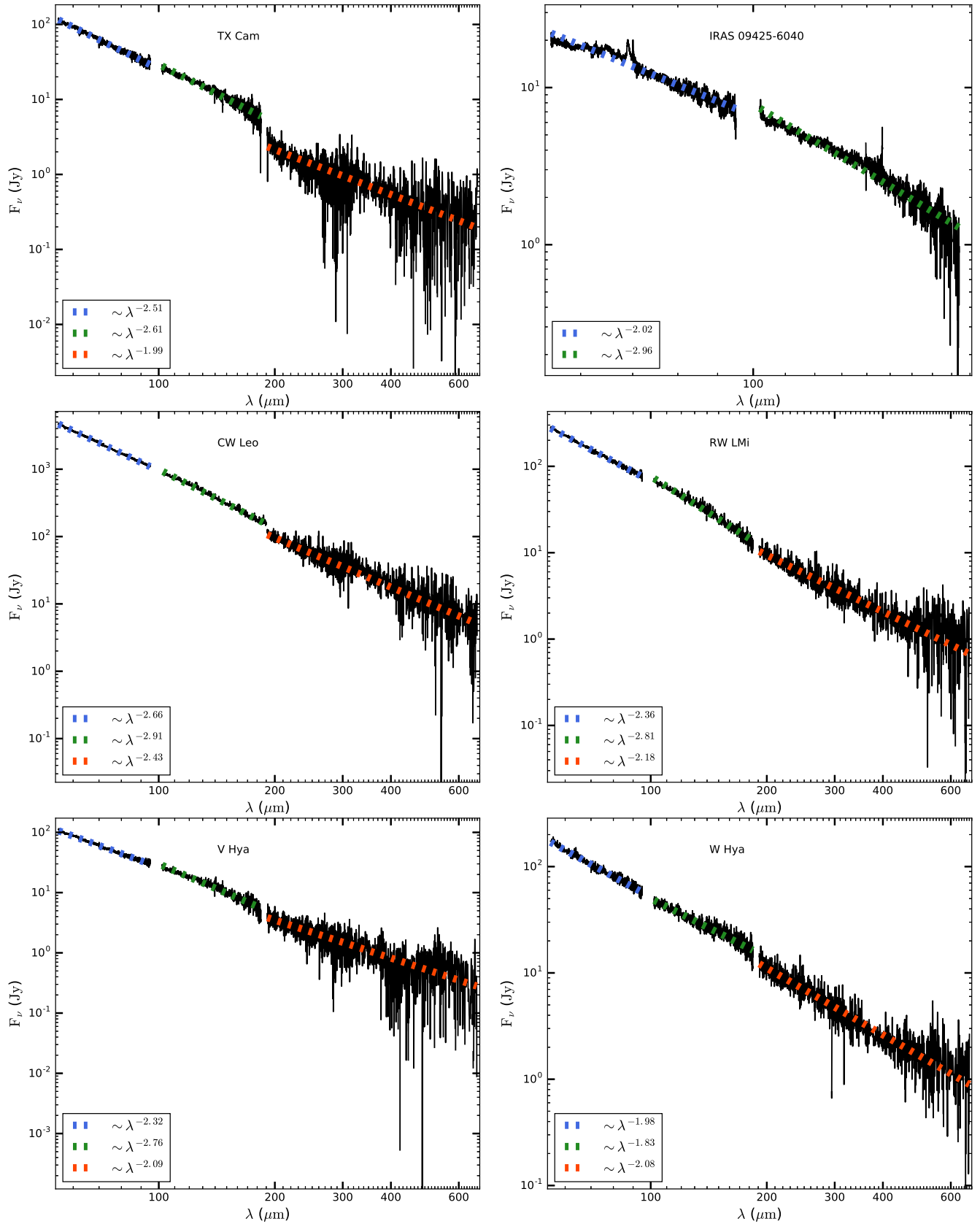


Fig. D.1. continued.

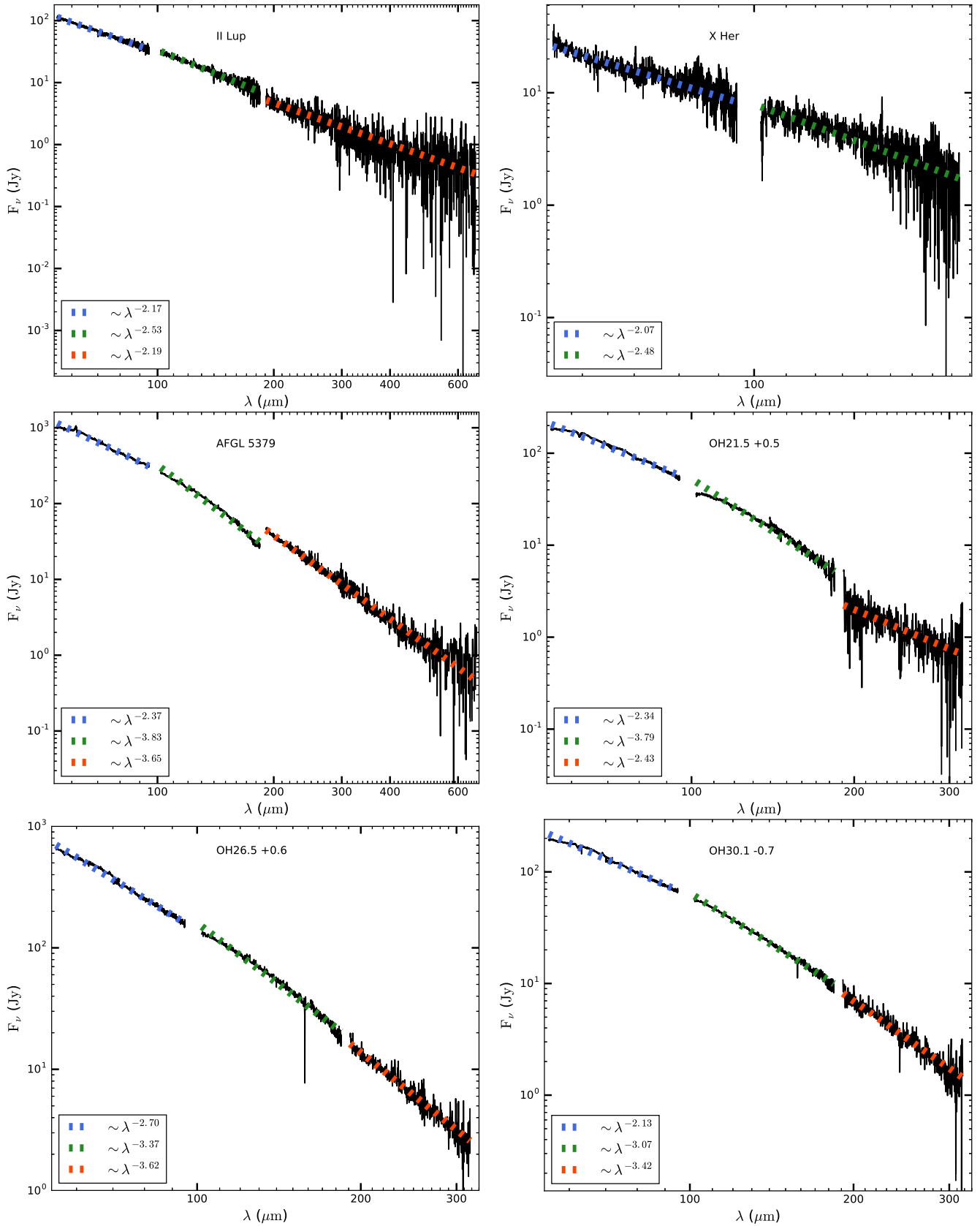


Fig. D.1. continued.

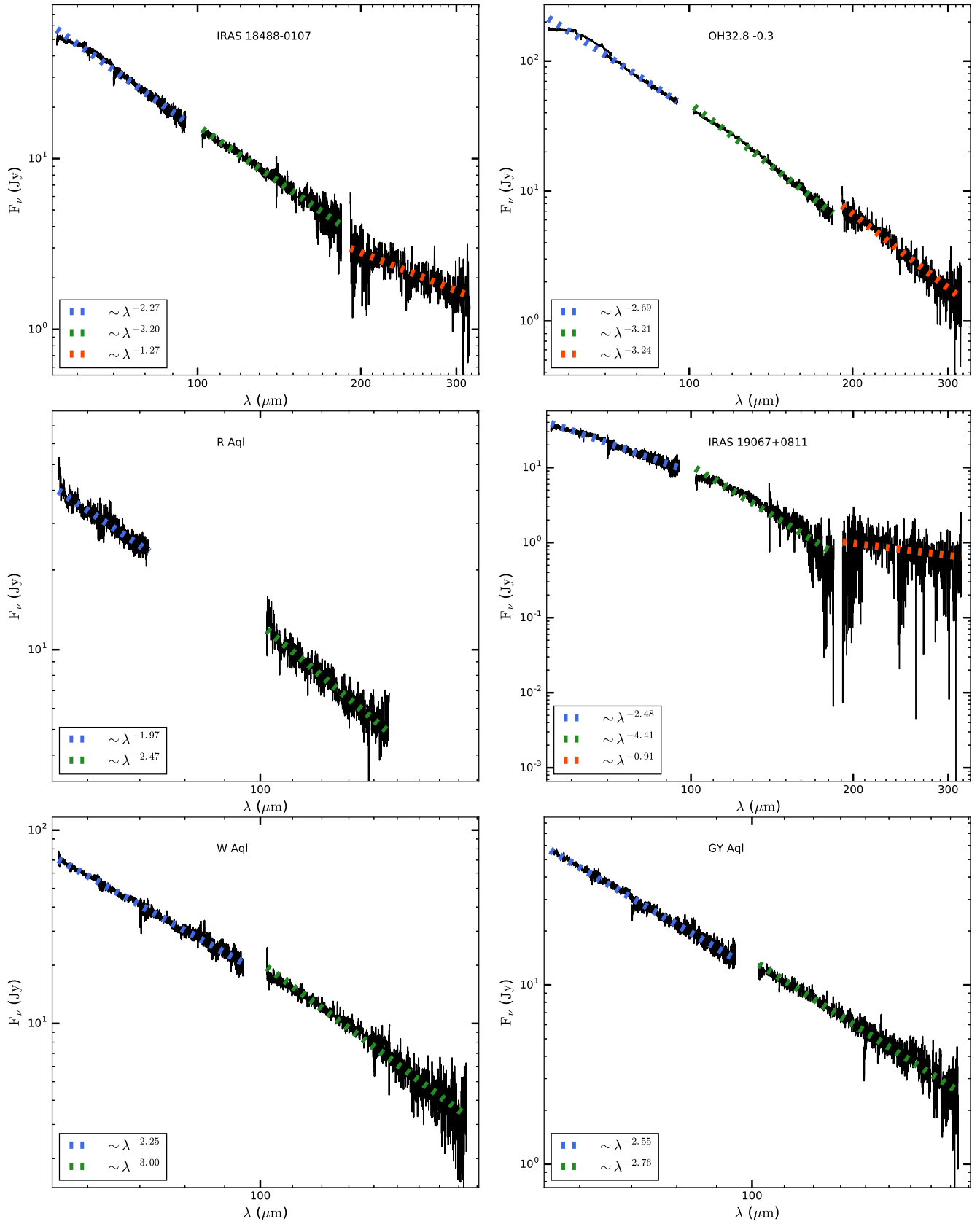


Fig. D.1. continued.

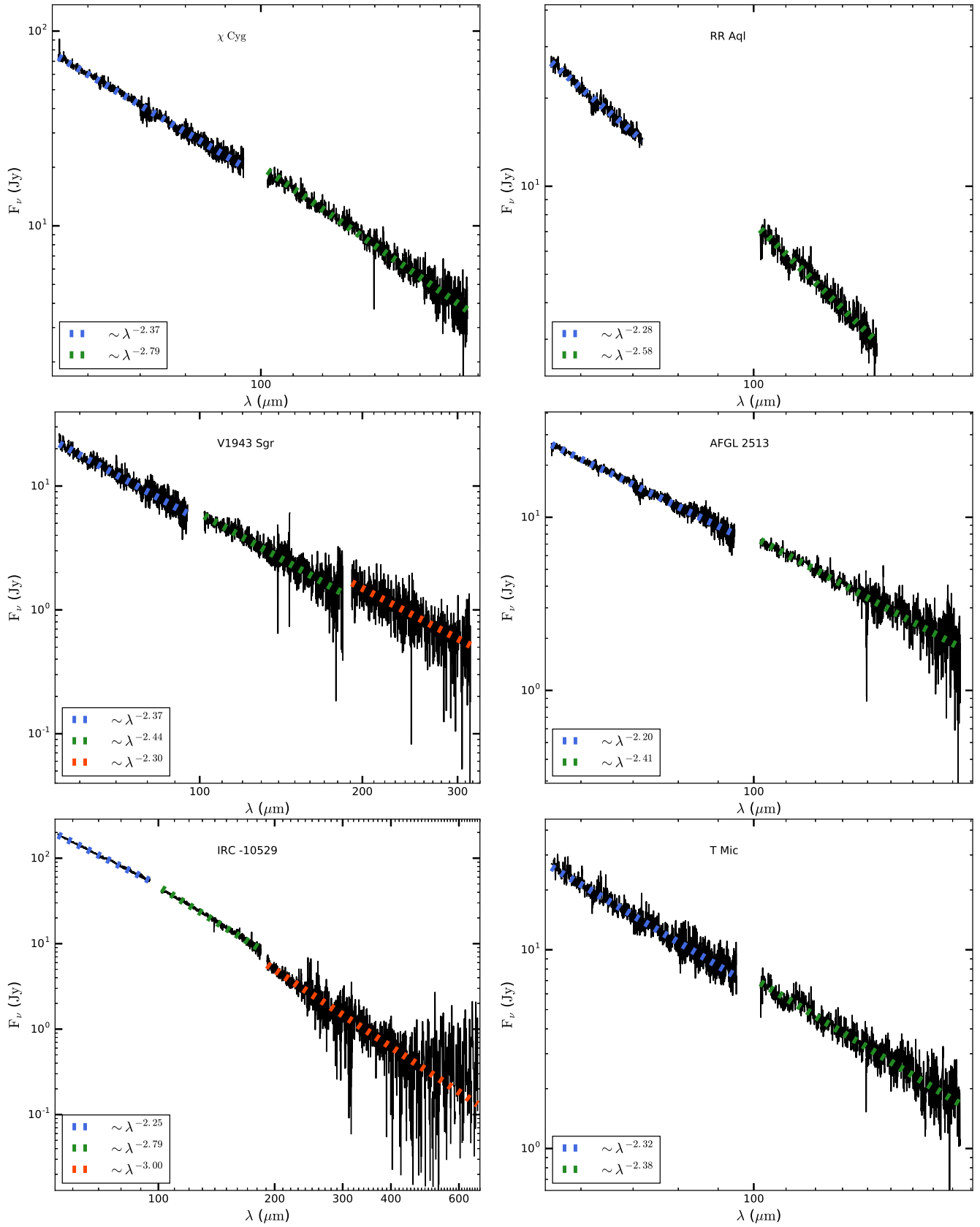


Fig. D.1. continued.

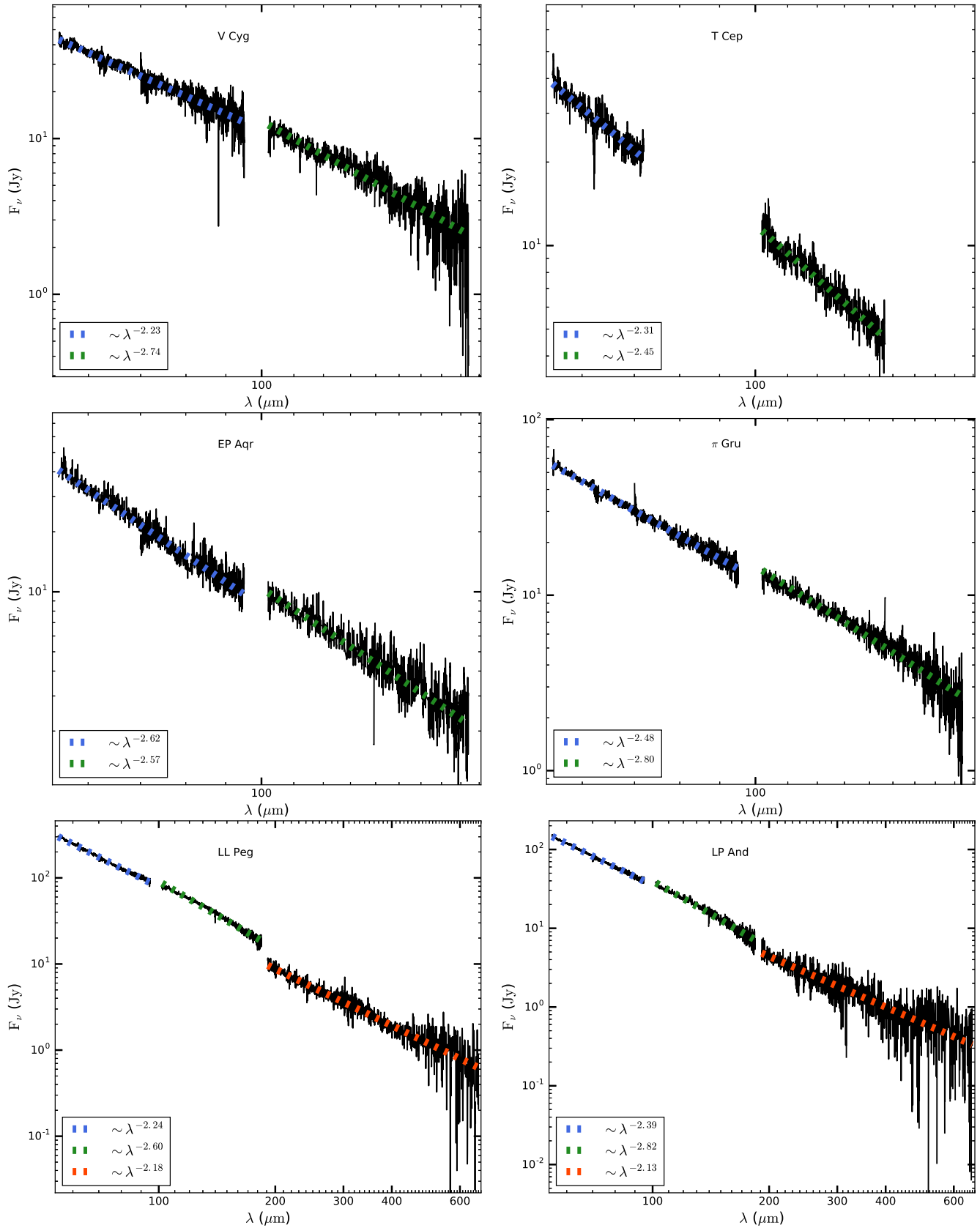


Fig. D.1. continued.

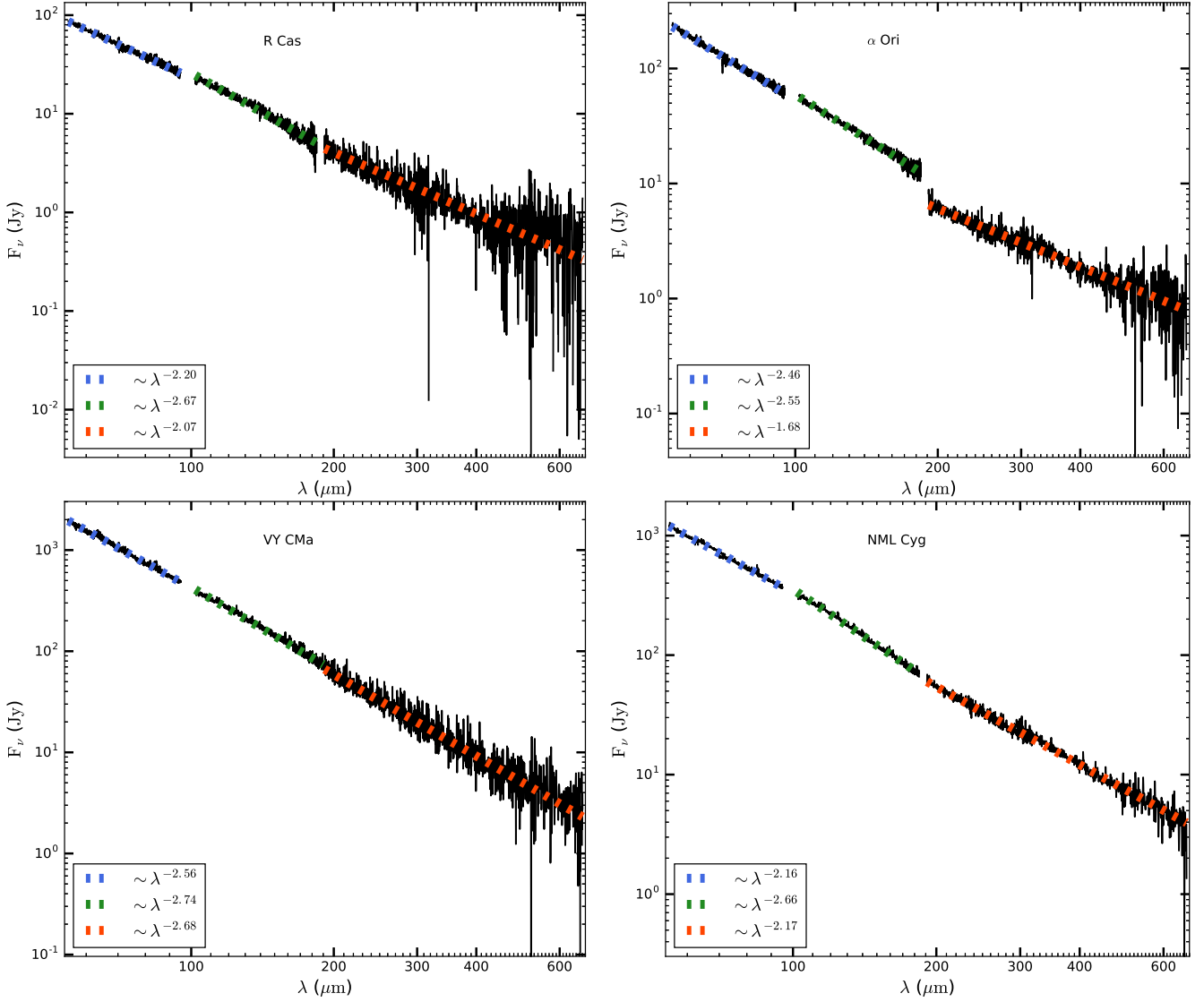


Fig. D.1. continued.

Appendix E: Line list and identification

This appendix gives the detected lines and the derived line fluxes following the methodology outlined in Sect. 4.1, and the possible line identifications as outlined in Sect. 4.2.

Table E.1 lists all the information. Only a portion of this table is shown here to demonstrate its form and content. The full table with all measured lines and possible line identifications for all targets is available at the CDS.

The first six columns are quantities that are derived from the spectra and the line fitting: the spectral band, observed wavelength and frequency, integrated line flux and error, and

the relative FWHM. The reported uncertainty in the line flux includes only the fitting uncertainty. The relative FWHM represents the measured width of the lines relative to the theoretical instrumental spectral resolution at the corresponding wavelength. High values can indicate possible broadening due to the blending of multiple molecular transitions. The next seven columns are related to the line identification: the molecular species and transition, the laboratory wavelength and frequency, and the contribution of that laboratory line to the observed line for temperatures of 75, 300, and 500 K assuming LTE and optically thin line emission (see Sect. 4.2 for details).

Table E.1. Integrated line strengths and possible identifications for selected spectral lines in WX Psc.

Band	λ_{obs} (μm)	ν_{obs} (GHz)	F_{int} (W m^{-2})	$\sigma(F_{\text{int}})$ (W m^{-2})	rel. fwhm	Species	Transition	λ_0 (μm)	ν_0 (GHz)	Con. 75 K (%)	Con. 300 K (%)	Con. 500 K (%)	
PACS													
B2A	55.82	5370.5073	2.60e-15	2.88e-16	3.142	H ₂ O	9 _{7,3} → 9 _{6,4}	55.76	5376.4121	<0.01	3.05	5.65	
						H ₂ O	11 _{7,5} → 11 _{6,6}	55.80	5372.7418	<0.01	0.41	2.00	
						H ₂ O	9 _{7,2} → 9 _{6,3}	55.80	5372.4280	<0.01	9.13	16.91	
						NH ₃	$J_{K_a, K_c} = 9_{8,1} \rightarrow 8_{8,0}$	55.81	5371.4285	99.28	1.29	<0.01	
						H ₂ O	10 _{2,9} → 10 _{1,10}	55.84	5368.8073	0.48	61.28	42.10	
						H ₂ O	8 _{7,2} → 8 _{6,3}	55.84	5368.6418	<0.01	18.27	22.19	
						H ₂ O	8 _{7,1} → 8 _{6,2}	55.85	5367.7484	<0.01	6.09	7.39	
						H ₂ O	12 _{7,6} → 12 _{6,7}	55.87	5366.2658	<0.01	0.35	3.02	
						NH ₃	$J_{K_a, K_c} = 9_{7,1} \rightarrow 8_{7,0}$	55.97	5355.9080	99.66	3.39	<0.01	
						H ₂ O	7 _{7,1} → 7 _{6,2}	55.98	5355.0246	0.02	14.91	16.56	
B2A	56.01	5352.9588	1.01e-15	2.04e-16	1.661	H ₂ O	7 _{7,0} → 7 _{6,1}	55.98	5354.8838	0.07	44.72	49.66	
						H ₂ O	10 _{1,9} → 10 _{0,10}	56.03	5350.8728	0.25	36.98	33.78	
						H ₂ O	9 _{1,9} → 8 _{0,8}	56.77	5280.7345	24.95	24.99	25.04	
						H ₂ O	9 _{0,9} → 8 _{1,8}	56.82	5276.5179	74.73	74.81	74.96	
						H ₂ O	4 _{2,2} → 3 _{1,3}	57.64	5201.4306	100.00	100.00	99.92	
						H ₂ O	2 _{2,1} → 1 _{1,0}	108.07	2773.9766	100.00	100.00	100.00	
						SO ₂	4 _{3,20,24} → 4 _{2,19,23}	108.72	2757.3522	<0.01	0.42	1.13	
						H ¹⁷ O	2 _{2,1} → 1 _{1,0}	108.74	2756.8424	49.98	37.93	12.82	
						H ¹⁸ O	2 _{2,1} → 1 _{1,0}	108.74	2756.8424	50.02	37.93	12.88	
						CO	24 → 23	108.76	2756.3876	<0.01	23.66	72.84	
R1 long	144.79	2070.5615	1.73e-16	1.25e-17	0.852	SiO, $\nu = 0$	48 → 47	144.75	2071.1379	<0.01	9.99	44.62	
						SO ₂	3 _{2,15,17} → 3 _{1,14,18}	144.78	2070.7199	0.67	1.95	0.94	
						SO ₂	2 _{7,16,12} → 2 _{6,15,11}	144.78	2070.6996	1.56	2.41	1.06	
						H ₂ S	3 _{2,1} → 2 _{1,2}	144.78	2070.6804	65.37	0.03	<0.01	
						CO	18 → 17	144.78	2070.6160	32.30	85.57	53.27	
	SPIRE												
	SSW	191.33	1566.9171	3.31e-17	3.49e-18	1.073	SO ₂	4 _{8,5,43} → 4 _{8,2,46}	191.27	1567.3843	0.14	1.37	1.15
							SO ₂	8 _{4,5,79} → 8 _{3,6,78}	191.30	1567.1178	<0.01	0.17	2.61
							SO ₂	8 _{5,5,81} → 8 _{4,4,80}	191.33	1566.8877	<0.01	0.18	2.93
							¹³ CS	34 → 33	191.34	1566.8118	0.10	10.81	16.02
						SO ₂	4 _{4,5,39} → 4 _{3,4,40}	191.34	1566.7757	17.05	29.04	19.38	
						SO ₂ , $\nu_2 = 1$	2 _{5,11,15} → 2 _{4,10,14}	191.35	1566.7451	0.53	33.71	36.42	
						SO ₂	4 _{0,4,36} → 3 _{9,3,37}	191.37	1566.5652	82.18	23.97	12.65	
						SO ₂	8 _{6,3,85} → 8 _{5,4,82}	191.38	1566.4728	<0.01	0.20	3.23	
						SO ₂	8 _{7,3,85} → 8 _{6,2,84}	191.40	1566.2905	<0.01	0.21	3.52	
						H ₂ O	6 _{3,3} → 5 _{4,2}	194.42	1541.9670	15.33	82.84	85.96	
SSW	194.47	1541.6022	8.11e-17	3.19e-18	0.996	¹³ CO	14 → 13	194.55	1540.9883	84.67	16.77	13.35	
						CO	12 → 11	216.93	1381.9951	100.00	99.82	99.56	
						H ₂ O	6 _{2,5} → 5 _{3,2}	226.76	1322.0648	43.26	94.77	95.81	
						¹³ CO	12 → 11	226.90	1321.2655	56.64	5.22	4.12	
						SO ₂	4 _{7,5,43} → 4 _{6,4,42}	294.92	1016.5113	0.71	46.00	53.66	
						SO ₂	3 _{2,17,15} → 3 _{3,16,18}	294.98	1016.3064	0.03	4.63	6.03	
						SO ₂	2 _{7,16,12} → 2 _{8,15,13}	295.01	1016.1947	0.38	6.46	6.30	
						¹³ CS	22 → 21	295.09	1015.9294	65.54	40.94	33.00	
						SO ₂	2 _{8,3,25} → 2 _{8,0,28}	295.10	1015.8995	33.34	1.98	0.91	

Appendix F: Atomic lines

In this appendix the presence of atomic lines in the PACS and SPIRE spectra is discussed. There is relatively little known about atomic lines around AGB stars. The C_I (1–0) line at $609\ \mu\text{m}$ has been detected in a few AGB stars using heterodyne techniques. The first detection of C_I in an AGB star was made by Keene et al. (1993) around CW Leo, and was confirmed by van der Veen et al. (1998). The modelling of these observations showed that the C_I is located in a shell (or shells) located at $\sim 14''$ (or larger). The same applies to the detection in R Scl (Olofsson et al. 2015) where the C_I is located in a shell at about $18''$. In both cases the origin of the atomic carbon is believed to be due to the photo dissociation of CO. Saberi et al. (2018) detected emission around *o* Ceti and confirmed the tentative detection in V Hya by Knapp et al. (2000). The emission in *o* Ceti is also believed to be in a shell located at $\sim 36''$, while Knapp et al. (2000) suggest shock dissociation of circumstellar CO (close to the star) for V Hya. Strong emission has been seen in α Ori (Huggins et al. 1994; van der Veen et al. 1998) believed to be related to the chromosphere in this supergiant. Non-detections have been reported for the following stars in our sample which have spectra: IK Tau and VY CMa (van der Veen et al. 1998).

Figure F.1 shows the region around the C_I (1–0) line at $609\ \mu\text{m}$ and the (2–1) line at $370\ \mu\text{m}$ for the stars discussed above. The spectrum used is the one that remains after removing all identified molecular lines, as described in Sect. 4.2 and Appendix E. No formal fitting has been attempted and the noise level can be judged from the spectral region shown.

The stars where previous analysis has shown that the atomic carbon is located in a shell (CW Leo, R Scl and *o* Ceti) are not detected. The surface brightness of the emission must be faint, and partly outside the central 3×3 spaxels. Emission is detected in the sources where previous analysis suggested that the C_I is located close to the central star (V Hya and α Ori)

The next two sources have been reported as non-detections from heterodyne observations and this is confirmed here (NML Tau and VY CMa). The remaining sources, OH 127.8, AFGL 5379, CIT 6, and AFGL 3068, appear to show one or both C_I lines, and are targets suggested for follow-up observations at higher spectral resolution.

The O_I lines at 63.2 and $145.5\ \mu\text{m}$ were also inspected but no obvious emission lines appear present. Finally, the C_{II} $157.7\ \mu\text{m}$ lines were plotted but no convincing emission lines were found, except some background subtraction problems in OH 30.1–0.7 and OH 26.5+0.6.

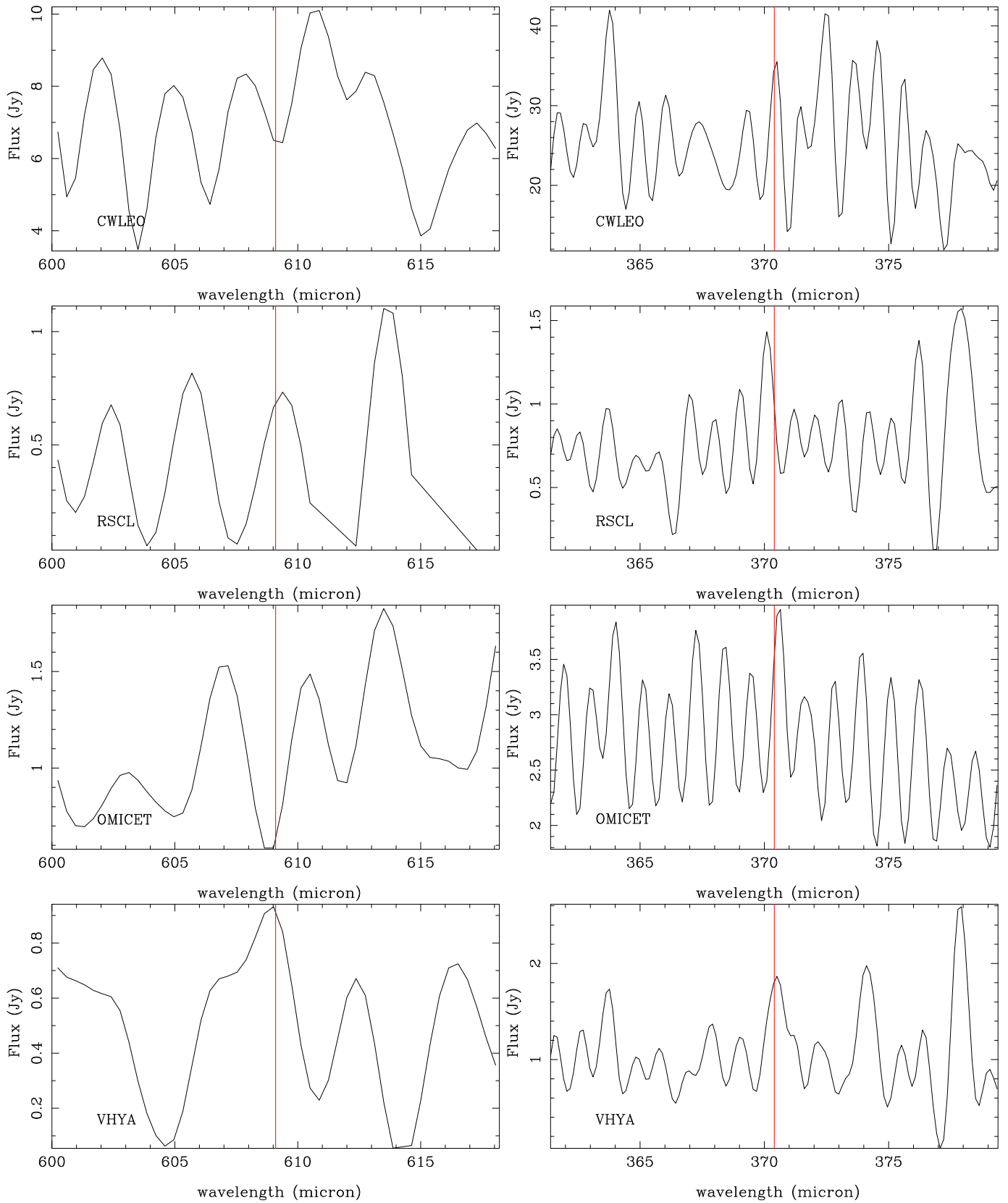


Fig. F.1. C I lines at 609 (left panels) and 370 μm (right panels). See text for comments on individual sources.

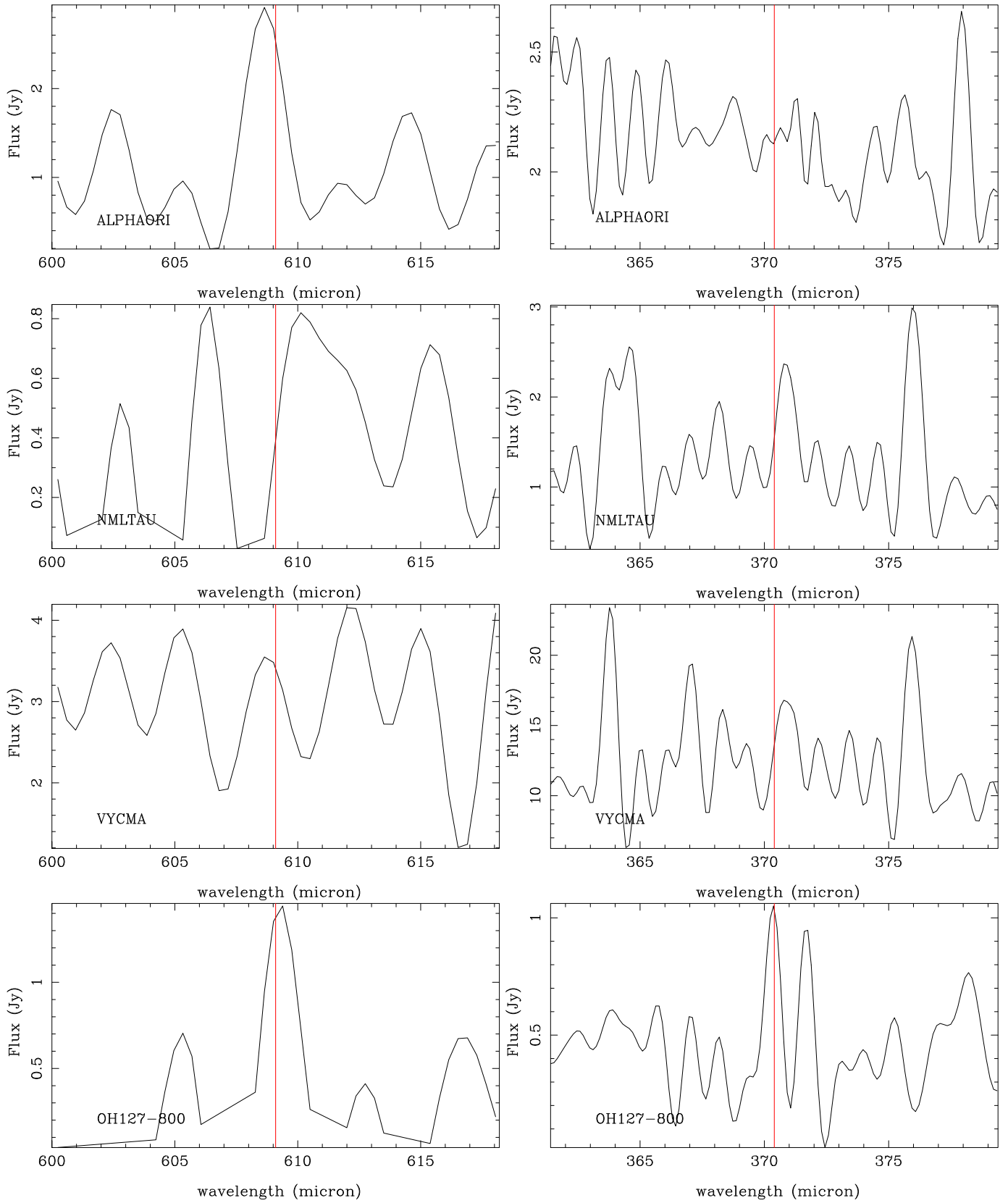


Fig. F.1. continued.

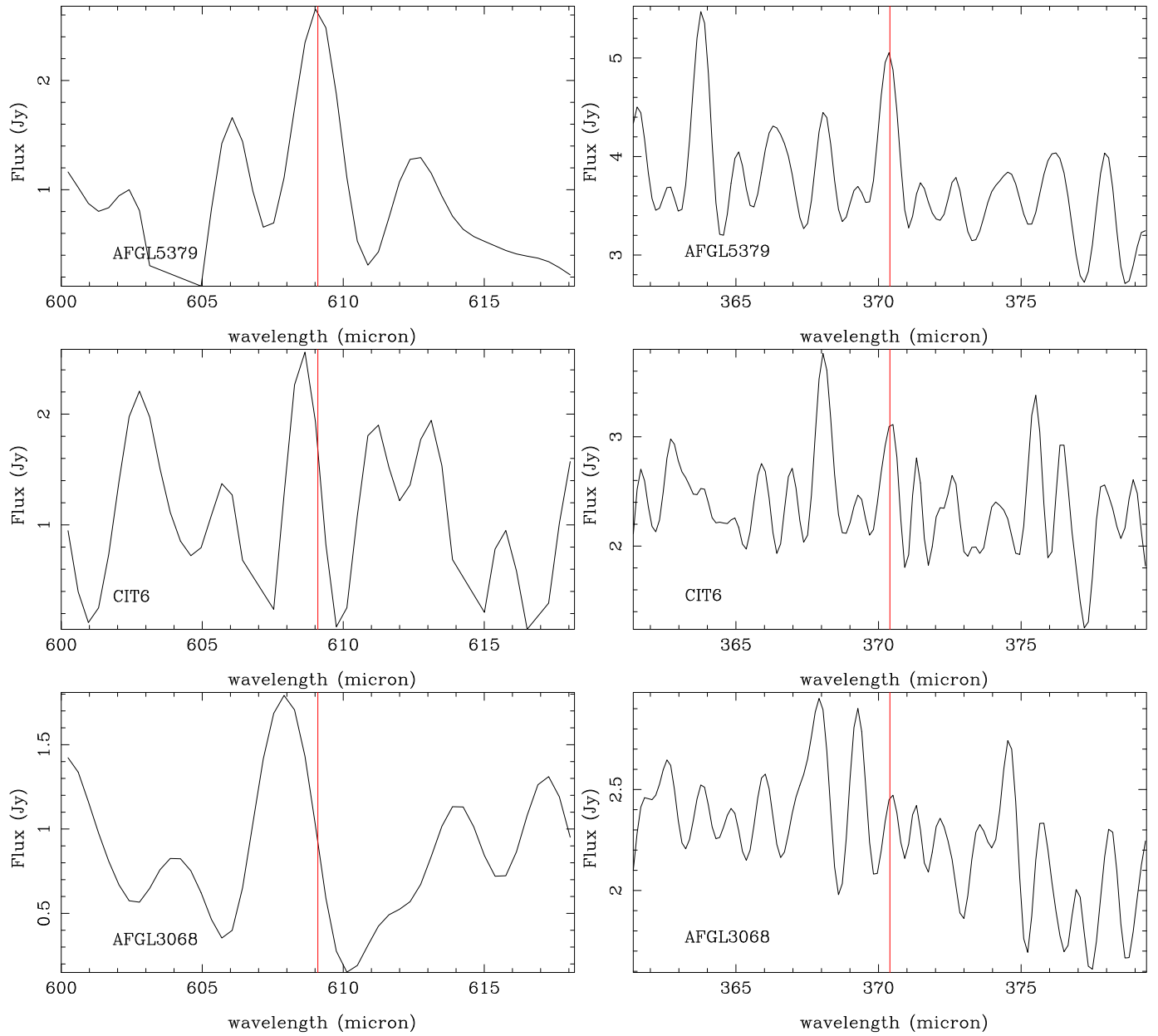


Fig. F.1. continued.